Numerical study on the response scenarios in a vibro-impact single-degree-of-freedom oscillator with two unilateral dissipative and deformable constraints

Giulia Stefani[a,*], Maurizio De Angelis[a], Ugo Andreaus[a]

[a]*Department of Structural and Geotechnical Engineering, "Sapienza" University of Rome, Via Eudossiana 18, 00184 Rome, Italy*

Abstract

In this paper, some of the scenarios that can occur in the numerical nonlinear non-smooth response of a vibro-impact single-degree-of-freedom system, symmetrically constrained by deformable and dissipative bumpers, were identified and described. The different scenarios, obtained varying selected dimensionless parameters, were investigated identifying homogeneous frequency intervals, characterized by similar features in terms of number and types of limit cycles, and resorting to phase portraits, basins of attraction and Fourier spectra. Despite the relative simplicity of the model, which however takes into account impact, clearance and unilaterality of the constraints, decreasing the dimensionless gap δ_0, from $\delta_0 = 1$ to $\delta_0 = 0$, gradually more complex and varied scenarios, characterized by different types of secondary resonances (with right or left hysteresis or of non-regular type), cascades in the low frequency range, periodic, quasi-periodic or chaotic solutions were observed. The occurrence of primary and secondary grazing was also highlighted.

Keywords: Regular and non-regular secondary resonances, Right and left hysteresis, Cascades, Primary and secondary grazing

1. Introduction

In many practical (biomedical, mechanical, civil, ...) engineering applications, mechanical components or structures repeatedly collide with one another or with obstacles [1]. Impacts occur, for example, in the capsule systems used in clinic endoscopy to inspect the surface lining of the intestine in the human body [2–6], and in the drilling rigs used in the oil and gas industry for creation of wells [7–12]. In the field of civil engineering, base-isolated systems (building [13–19], bridges [20–22], equipment [23–28], strategic facilities [29]) when subject to exceptional loads, like severe earthquakes, can undergo large horizontal displacements, concentrated in the isolation system. These displacement can damage the isolation system itself or can lead to pounding between the isolated system and the surrounding moat walls or any adjacent structures, if the available surrounding gap is not sufficient. The consequences of pounding can damage the structure or sensitive equipment housed in it, impairing their functionality. When it is not possible to guarantee a sufficient clearance, the side effects of pounding can be mitigated reducing the impact stiffness through the interposition of dissipative and deformable shock absorbers (also known as bumpers) between the colliding systems [30, 31]. In the absence of obstacles near the isolated system, to avoid the excessive deformation or the damage of the isolation system, the displacements can be limited either by inserting end stops or by using other suitable types of control systems [32–34].

Several scientific works, of both numerical and experimental nature, dealt with vibro-impact dynamics. In the numerical simulations impact can be modeled using both a stereomechanical or a force-based approach [35]. In the first approach, the duration of the contact is neglected and the impact is modeled using the momentum conservation

*Corresponding author

Email addresses: giulia.stefani@uniroma1.it (Giulia Stefani), maurizio.deangelis@uniroma1.it (Maurizio De Angelis), ugo.andreaus@uniroma1.it (Ugo Andreaus)

principle and the coefficient of restitution, the latter defined as the ratio between the velocities immediately after impact and immediately before the impact [36]. In the second approach, the contact force can be modeled in different ways, resorting to more or less sophisticated modeling [37–41], going from pure elastic contact force models, such as the linear spring element and the Hertz contact model (nonlinear spring element [42, 43]), which however do not take into account the energy loss during the impact, to dissipative contact force models, such as the Kelvin-Voigt model [36, 44, 45] and the model proposed by Hunt and Crossley [46], to overcome the drawbacks of the Kelvin-Voigt model, and consisting of an elastic Hertz's law combined with a nonlinear viscoelastic element (Hertzdamp model).

The types of impact motion, and the bifurcations from one motion to the other, that can occur in the dynamics of vibro-impact systems with motion limiting constraints, with the variation of selected parameters are the subject of several studies, of mainly numerical nature [47–60]. The study of the dynamics of a two-degree-of-freedom periodically-forced system with symmetric motion limiting constraints, with emphasis on the transition between fundamental impact motions, together with the design and implementation of an electronic circuit, describing the dynamic characteristics of the non-smooth system, are presented in [52]. The motions of a periodically forced non-smooth Duffing system at the switching boundary and the coexistence of different attractors are investigated in [56] through numerical simulations. Focusing on the switching behaviors on the boundary between two adjacent domains, in a periodically forced modified Duffing-Rayleigh system, the coexistence of attractors, under different initial conditions, is illustrated through basins of attraction and phase planes in [60]. The grazing-induced bifurcations in impact oscillators with one-sided elastic and rigid constraints are investigated and classified in [53] by a path-following method. In [58], pattern types, stability domains and bifurcation characteristics of periodic motions for a two-degree-of-freedom oscillator with a clearance are investigated and attracting domains and Poincaré mapping diagrams of coexisting motions in the neighborhood of grazing bifurcations are discussed. The parameters influence and the features of the dynamic response of impact oscillators in the vicinity of degenerate grazing points is investigated and characterized in [59], using the GPU computing parallel technology and other numerical methods. Phenomena of coexisting attractors and chaotic transitions, including crisis, are also discussed, considering single and two degree-of-freedom impact oscillators.

The practical problem of base-isolated structures impacting against moat-walls inspired several works of the authors, of both numerical and experimental nature, in which the response of these structures was simulated using a single-degree-of-freedom (SDOF) oscillator, consisting of a mass and a damper, impacting against two deformable and dissipative constraints (bumpers), symmetrically arranged on both sides [61–69]. Some of the scenarios that can occur within the system response were first investigated in the theoretical-numerical work presented in [61]. The study of the scenarios was then taken up by the authors in [68, 69], in which some scenarios, identified based on the results of an experimental laboratory campaign, were investigated and then reproduced using a suitable numerical model.

Based on the results obtained in [68, 69], the aim of the present work is to deepen the study of the scenarios that can occur in the nonlinear non-smooth response of a vibro-impact single-degree-of-freedom (SDOF) system, from a numerical point of view, extending the range of investigated parameters, compared to the previous studies. The system, symmetrically constrained with deformable and dissipative bumpers, and subject to a sine sweep base excitation, is described in terms of dimensionless parameters and particular attention is devoted in this work to the study of the role played by the damping ratio, due to the adopted normalization. The scenarios are identified based on the characteristics of the Pseudo-Resonance Curves (PRCs) of normalized excursion and eccentricity of absolute acceleration and relative displacement of the mass. The scenarios observed by reducing the dimensionless gap and keeping the values of the other dimensionless parameters fixed, are subsequently investigated by identifying homogeneous frequency ranges and resorting to phase portraits, basins of attraction and Fourier spectra.

The paper is organized as follows. The numerical model of the nonlinear SDOF system, together with the dimensionless governing equations and the study on the role of damping, are introduced in Sect. 2; the identified scenarios are shown and discussed in Sect. 3; the conclusions and future developments of the work are finally drawn in Sect. 4.

2. Numerical model

A suitable numerical model, able to simulate the dynamic behavior of a vibro-impact single-degree-of-freedom SDOF system, impacting against unilateral dissipative and deformable obstacles (bumpers), is shown in Fig. 1. The system consists of a mass M and a damper (D), the latter modeled by a linear elastic element, with stiffness K, and a linear viscous damper, with damping coefficient C, arranged in parallel. The two obstacles, denoted as right bumper (B_R) and left bumper (B_L) respectively, are symmetrically positioned on both sides of the mass, at an initial distance

(initial gap) G_{0j} (j = R, L), are massless and are modeled by a linear elastic element, with stiffness K_j (j = R, L), and a linear viscous damper, with damping coefficient C_j (j = R, L), arranged in parallel. The system is subject to a harmonic base acceleration $A_t(t) = A_G \sin \Omega t$, with amplitude A_G and circular frequency Ω. In Fig. 1, u and u_j (j = R, L) denote the displacements, of the mass and of the two bumpers respectively, relative to the ground.

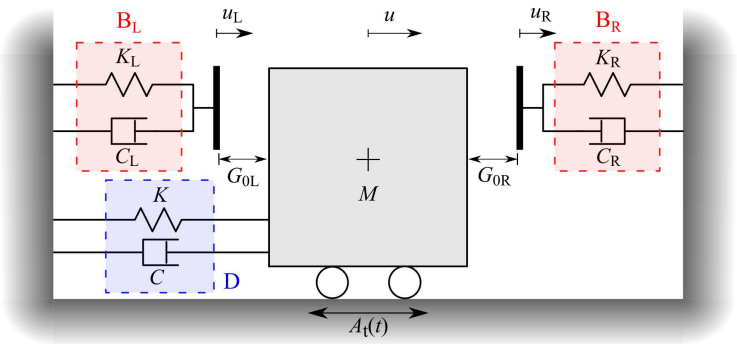

Figure 1: Model of the system.

2.1. Dimensionless equations of motion

The equations of motion of the system depicted in Fig. 1 can be written in the following dimensionless form:

$$\begin{cases} q''(\tau) + 2\xi q'(\tau) + r(\tau) + \left[2\xi\gamma_j q'(\tau) + r_j(\tau)\right] \cdot \psi_1\left[\delta_j(\tau)\right] \cdot \psi_2\left[f_j(\tau)\right] = -a_G \sin\beta\tau \\ 2\xi\gamma_i q'(\tau) + r_i(\tau) = 0 \end{cases} \tag{1}$$

In Eq. (1), it is assumed that whether j = L then i = R, or whether j = R then i = L. The nondimensionalization of the governing equations was obtained by introducing the following characteristic quantities:

$$\omega = \sqrt{\frac{K}{M}}, \quad u^* = \frac{MA_G}{K} R_{d,max}, \quad F^* = Ku^* = M\omega^2 u^* = MA_G R_{d,max} \tag{2}$$

namely the natural circular frequency of the SDOF system ω, the maximum relative displacement u^* and the maximum force F^* in the SDOF system in free flight (that is without obstacles) resonance condition. In Eq. (2), $R_{d,max}$ is the maximum value of the dynamic amplification factor R_d,defined as the ratio between the amplitude of the dynamic displacement u to the static displacement MA_G/K, at the resonant frequency, which is function of the damping ratio $\xi = C/(2M\omega)$ of the SDOF system, that is $R_{d,max} = 1/(2\xi\sqrt{1-\xi^2})$ for $\xi < \sqrt{2}/2$. In Eq. (1), $q = u/u^*$ and $q_j = u_j/u^*$ (j = R, L) are the dimensionless relative displacements of the mass and of the right and left bumper respectively, and the apex ($'$) denotes differentiation with respect to the dimensionless time $\tau = \omega t$; $a_G = 2\xi\sqrt{1-\xi^2}$ is the dimensionless amplitude of the base acceleration $a_t(\tau)$; $\beta = \Omega/\omega$ is the ratio between the circular frequency of the base excitation Ω and the natural circular frequency of the SDOF system ω; $\gamma_j = C_j/C$ (j = R, L) is the ratio between the viscous damping coefficients of the j-th bumper and that of the damper and $\delta_j(\tau)$ is the clearance function that represents the distance, instant by instant, between the mass and the j-th bumper and it is defined as follows:

$$\delta_j(\tau) = \delta_{0j} + \Delta q_j(\tau) \quad (j = R, L) \tag{3a}$$

$$\Delta q_R(\tau) = q_R(\tau) - q(\tau), \quad \Delta q_L(\tau) = q(\tau) - q_L(\tau) \tag{3b}$$

When the mass is in contact with the j-th bumper $\delta_j(\tau) = 0$ (j = R, L), otherwise $\delta_j(\tau) > 0$. In Eq. (3a) $\delta_{0j} = G_{0j}/u^*$ (j = R, L) denotes the initial dimensionless gap between the mass and the j-th bumper. Based on the adopted normalization, $\delta_{0j} = 0$ if the j-th bumper is initially in contact with the mass; for $0 < \delta_{0j} < 1$ the mass beats

and deforms the j-th bumper; whereas the mass will be in free flight condition for $\delta_{0j} \geq 1$. In Eq. (1), ψ_1 and ψ_2 represent the Heaviside functions, defined as follows:

$$\text{Approaching contact} \quad \psi_1\left[\delta_j(\tau)\right] = \begin{cases} 0, & \delta_j(\tau) > 0 \\ 1, & \delta_j(\tau) = 0 \end{cases} \tag{4a}$$

$$\text{Separation} \quad \psi_2\left[f_j(\tau)\right] = \begin{cases} 0, & f_j(\tau) \leq 0 \text{ (j = R)} \quad \text{or} \quad f_j(\tau) \geq 0 \text{ (j = L)} \\ 1, & f_j(\tau) > 0 \text{ (j = R)} \quad \text{or} \quad f_j(\tau) < 0 \text{ (j = L)} \end{cases} \tag{4b}$$

where $f_j(\tau) = 2\xi\gamma_j q'(\tau) + r_j(\tau)$ is the contact force occurring during the contact period with the j-th bumper. The normalized restoring forces, exerted by the damper and the bumpers, were denoted by r and r_j (j = R, L) respectively, and they have the following expressions:

$$r(\tau) = q(\tau) \tag{5a}$$

$$r_R(\tau) = \lambda_R q_R(\tau) = \lambda_R[q(\tau) - \delta_{0R}], \quad r_L(\tau) = \lambda_L q_L(\tau) = \lambda_L[q(\tau) + \delta_{0L}] \tag{5b}$$

where $\lambda_j = K_j/K$ (j = R, L) is the ratio between the stiffnesses of the j-th bumper and that of the damper.

2.2. Parameters

The dimensionless parameters that influence the response of the system are therefore: the frequency ratio β, the damping ratio ξ, the initial dimensionless gap δ_{0j} (j = R, L), the stiffness ratio λ_j (j = R, L) and the damping ratio γ_j (j = R, L). As an alternative to the damping ratio γ_j, the dissipative capacities of the bumpers can also be characterized through the dimensionless relaxation time $\tau_{rj} = \omega\, t_{rj}$, where $t_{rj} = C_j/K_j$ (j = R, L). In this study we considered two equal bumpers symmetrically arranged on the two sides of the mass. It follows that $\lambda_R = \lambda_L = \lambda$, $\gamma_R = \gamma_L = \gamma$ (or alternatively $\tau_{rR} = \tau_{rL} = \tau_r$) and $\delta_{0R} = \delta_{0L} = \delta_0$.

2.3. Nonlinearities

Although both the bumpers and the damper have been modeled with a linear elastic spring in parallel with a linear viscous dashpot, the system is however strongly nonlinear. In particular, the nonlinearities are due to the presence of clearance, the unilateral constrains and the occurrence of impact that causes abrupt changes of stiffness and damping at the contact time.

2.4. Role of damping

The damping ratio of the SDOF system ξ affects both the response of the system (it reduces the response amplitude at all excitation frequencies) and, following the adopted normalization, the amplitude of the base acceleration a_G. In the absence of bumpers, by normalizing the amplitude of dynamic displacement u with respect to the maximum displacement in resonance condition u^*, instead of the static displacement, the dynamic amplification factor (denoted as R to distinguish it from R_d [70]), function of both damping ratio ξ and frequency ratio β, for $\xi < \sqrt{2}/2$, is given by:

$$R(\xi,\beta) = \frac{2\xi\sqrt{1-\xi^2}}{\sqrt{(1-\beta^2)^2 + (2\xi\beta)^2}} \tag{6}$$

In Fig. 2, $R(\xi,\beta)$ is plotted for different values of damping ratio ξ. It can be observed that, for $\beta = 0$ (slowly varying excitation), R (Eq. (6)) attains the value $R(\xi,0) = 2\xi\sqrt{1-\xi^2}$ and thus it increases with ξ, as long as $0 < \xi < \sqrt{2}/2$; for $\sqrt{2}/2 \leq \xi < 1$, $R(\xi,0) = 1$. The variation of the resonant frequency ratio $\beta_{res} = \sqrt{1-2\xi^2}$ with ξ is highlighted with black dots. It can be noted that β_{res} decreases as ξ increases and, for $\sqrt{2}/2 \leq \xi < 1$, $\beta_{res} = 0$.

In the presence of bumpers, symmetrically placed at an initial distance δ_0, impact can occur. In particular, it is possible to analytically determine the frequency interval in which impact surely will occur, for a given value of δ_0, by imposing:

$$R(\xi,\beta) = \frac{2\xi\sqrt{1-\xi^2}}{\sqrt{(1-\beta^2)^2 + (2\xi\beta)^2}} = \delta_0 \tag{7}$$

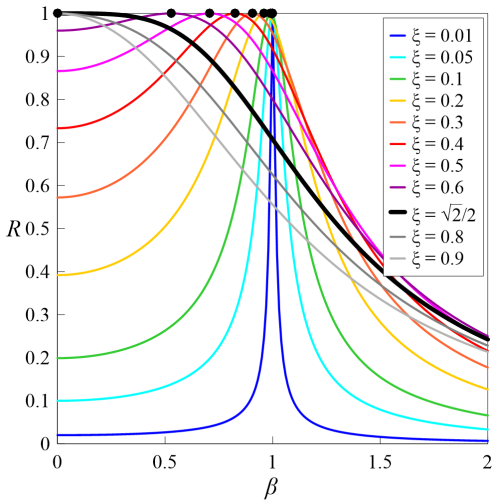

Figure 2: Dynamic amplification factor $R(\xi,\beta)$ for different values of the damping ratio ξ.

By solving Eq. (7), for each (ξ, δ_0) pair in the ranges $0 < \xi < 1$ and $0 \leq \delta_0 \leq 1$, the contour maps of the roots, denoted as β_1 (red) and β_2 (blue) respectively (with $\beta_2 \geq \beta_1$), shown in Fig. 3(a), were obtained. It can be observed that the $\delta_0 - \xi$ plane is divided in two regions by the thick green curve with equation $\delta_0 = 2\xi\sqrt{1-\xi^2}$ (for $0 < \xi < \sqrt{2}/2$). Along this curve, $\beta_1 = 0\ \forall\xi$, whereas β_2 decreases as ξ increases. In the region above this curve, the two contour maps associated with the two roots of Eq. (7), β_1 and β_2, overlap. In the region below this curve, there is only the contour map associated with β_2.

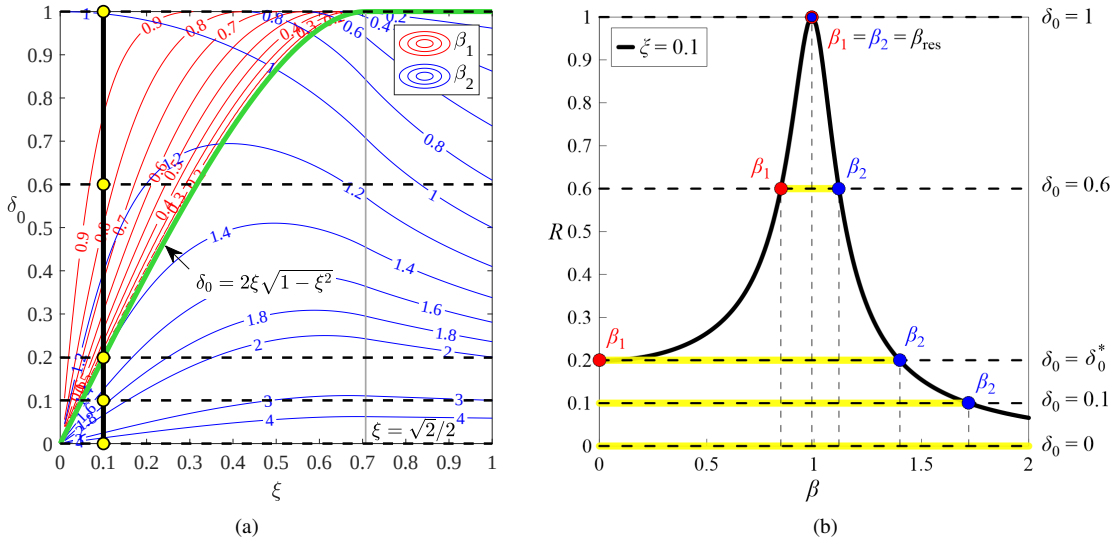

Figure 3: a) Contour maps of the frequency ratios β_1 (red) and β_2 (blue) in the $\xi - \delta_0$ plane; b) dynamic amplification factor R for $\xi = 0.1$ with the location of β_1 (red) and β_2 (blue) corresponding to the considered δ_0 values (horizontal dashed lines). The frequency interval between β_1 and β_2 (highlighted in yellow) is characterized by the occurrence of impact.

For a given value of damping ratio, for example $\xi = 0.1$ (see the thick black vertical line in Fig. 3(a) and the corresponding dynamic amplification factor $R(0.1,\beta)$ in Fig. 3(b)), different situations can occur depending on the value of δ_0 (yellow dots in Fig. 3(a)). It can be observed that:

- For $\delta_0 = 1$, Eq. (7) admits two coincident roots $\beta_1 = \beta_2 = \beta_{\text{res}}$; consequently, impact does not occur for any β

value;

- For $\delta_0^* = 2\xi\sqrt{1-\xi^2} < \delta_0 < 1$, e.g. $\delta_0 = 0.6$, Eq. (7) admits two non-zero roots, $\beta_1 < \beta_{res}$ and $\beta_2 > \beta_{res}$; these two roots approach as δ_0 increases;
- For $\delta_0 = \delta_0^* = 2\xi\sqrt{1-\xi^2}$, e.g. $\delta_0 \simeq 0.2$, Eq. (7) admits two roots: $\beta_1 = 0$ and $\beta_2 > \beta_{res}$;
- For $0 < \delta_0 < \delta_0^* = 2\xi\sqrt{1-\xi^2}$, e.g. $\delta_0 = 0.1$, Eq. (7) admits a single non-zero root ($\beta_2 > \beta_{res}$), whose value decreases with increasing δ_0;
- For $\delta_0 = 0$, $R(\xi,\beta) > \delta_0 \ \ \forall\beta$; consequently, Eq. (7) does not admit roots; this means that impact always occurs independently of β.

In Fig. 3(b), for each considered δ_0 value, the frequency interval in which impact will surely occur ($\beta_1 \leq \beta \leq \beta_2$) was highlighted with a yellow horizontal line. It can be observed that, this frequency range increases as δ_0 decreases. It is worth noting that impact can also occur for $\beta < \beta_1$ or $\beta > \beta_2$, depending on the nonlinear behavior of the system, the values of the parameters and the initial conditions. The same considerations apply for other values of damping ratio $0 < \xi < \sqrt{2}/2$; what changes is the value of δ_0^* and consequently the amplitudes of δ_0 intervals in which there is only the root β_2 (below the green curve in Fig. 3(a)) or both roots β_1 and β_2 (above the green curve in Fig. 3(a)). For $\sqrt{2}/2 \leq \xi < 1$, Eq. (7) admits a single non-zero root ($\beta_2 > 0$) $\forall\delta_0 \in]0;1[$, whereas for $\delta_0 = \delta_0^* = 1$, the two roots are coincident and equal to zero ($\beta_1 = \beta_2 = 0$). As concerns the amplitude of the base excitation, since the system is nonlinear, it can significantly affect the dynamical phenomena exhibited by the system. Due to the adopted normalization, it depends on the damping ratio ξ ($a_G = 2\xi\sqrt{1-\xi^2}$) and varies with the same law shown by the thick green curve in Fig. 3(a). It can be observed that a_G increases with ξ, as long as $\xi < \sqrt{2}/2$; whereas, for $\sqrt{2}/2 \leq \xi < 1$, it is independent from ξ and it is equal to 1. Consequently, the parameter that describes the input is not what is expected (its amplitude), but rather the damping ratio ξ. The excitation, thus is essentially filtered through the damping ratio. In this paper we assumed $\xi = 0.1$, which corresponds to a_G almost equal to 0.2. This study on the role of damping ξ and on the evolution of the roots of Eq. (7) with the dimensionless gap δ_0 (Fig. 3(b)) guided the subsequent numerical investigations and, thus, it is functional to what will be said in the following Sections.

3. Scenarios

In this Section, some of the scenarios that can occur in the dynamic non-smooth response of the SDOF system, with the variation of selected parameters, will be identified and discussed. In particular, the analyses were conducted by assuming $\xi = 0.1$ and $\gamma = 5$, and by varying λ and δ_0. The authors do not claim to have exhaustively identified all the possible scenarios that can occur; those shown are just some of situations emerged in this exploratory numerical investigation. The identification of the scenarios was made on the basis of the characteristics of the Pseudo-Resonance Curves (PRCs) of normalized excursion and eccentricity of relative displacement ($\eta_d = \Delta q/\Delta q_0$ and $e_d = \overline{q}/\Delta q_0$ respectively) and absolute acceleration ($\eta_a = \Delta a/\Delta a_0$ and $e_a = \overline{a}/\Delta a_0$ respectively) of the mass. The PRCs were obtained considering a step-wise forward and backward sine sweep base acceleration, that is a harmonic signal with constant amplitude, in which the forcing frequency is increased (forward sweep) and then decreased (backward sweep) over time, within a specific frequency range and with an appropriate frequency increment, after a certain number of cycles. Subsequently, based on the results obtained with the sine sweep signal, in cases where it was considered necessary, further in-depth analyses on the influence of initial conditions, with the construction of basins of attraction, were carried out. The absolute acceleration of the mass $a(\tau)$ is given by the sum of the acceleration of the ground $a_t(\tau)$ and the relative acceleration between the mass and the ground $q''(\tau)$: $a(\tau) = a_t(\tau) + q''(\tau)$. The excursion ($\Delta q$ and Δa) was calculated as the difference between the maximum and minimum values recorded at steady-state of each sub-frequency range, that is $\Delta q = q_{max} - q_{min}$ and $\Delta a = a_{max} - a_{min}$, whereas the eccentricity ($\overline{q}$ and $\overline{a}$) was calculated as the half-sum of maximum and minimum values, that is $\overline{q} = (q_{max} + q_{min})/2$ and $\overline{a} = (a_{max} + a_{min})/2$ and thus, it allowed to highlight non symmetric behaviors. Subsequently, both the excursion and the eccentricity, thus calculated, were normalized with respect to the maximum excursion in free flight resonant condition (Δq_0 and Δa_0 respectively). Referring to the situation characterized by the presence of the obstacles, initially placed at a distance δ_0 from the mass, in order to classify the scenarios from the characteristics of PRCs, a first distinction was made on the basis of

the absence ($\delta_0 \geq 1$) or occurrence ($0 \leq \delta_0 < 1$) of impact. In the latter case, a further differentiation was made based on the absence or existence of the *primary resonance with right hysteresis*, between the jumps in the forward and backward sweeps. Finally, the occurrence and type of *secondary resonances* in the low frequency range, and the existence of frequency ranges characterized by non-zero eccentricity allowed to recognize further scenarios. This procedure made it possible to identify, in the $\lambda - \delta_0$ plane, for $0 \leq \delta_0 \leq 1$ and $0 < \lambda \leq 100$, seven homogeneous regions, identified by Roman numerals enclosed within circles and highlighted with different colors in the map shown in the central part of Fig. 4.

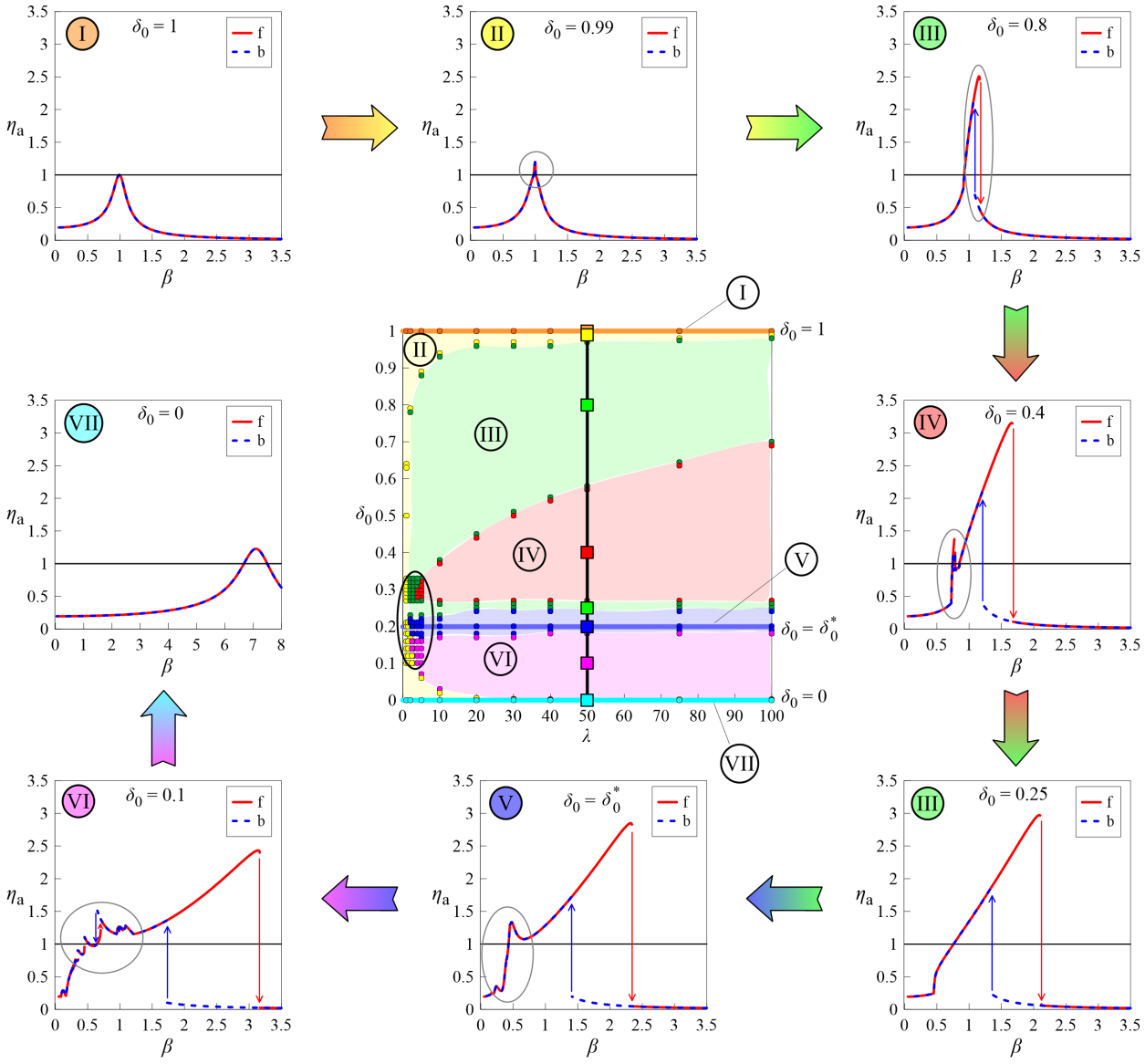

Figure 4: Homogeneous regions in the $\lambda - \delta_0$ plane ($\xi = 0.1$, $\gamma = 5$), identified by Roman numerals enclosed within circles and highlighted with different colors. The colored dots represent the $\lambda - \delta_0$ pairs investigated to qualitatively identify the boundaries of the regions. Representative PRCs of η_a for $\lambda = 50$ (vertical black line), corresponding to the colored squares, are arranged clockwise around the map.

The colored dots represent some of the (λ, δ_0) pairs investigated to qualitatively identify, in a discrete way, the boundaries of these regions. These borders should not be seen as well-defined dividing lines, but rather as thick blurred lines, because the transition from one region to another occurs with gradual evolutions. For small values of λ

and δ_0 (see the region enclosed by an ellipse), a high density of investigated points is observed. In this zone, which will not be investigated in this work, some of the identified regions converge (high chromatic variety), and thus, small variations in both λ and δ_0 determine the passage from one region to another. From Fig. 4, it can be observed that two of the identified regions are more properly lines, namely $\delta_0 = 1$ (Region I, highlighted with an horizontal orange line), and $\delta_0 = 0$ (Region VII, highlighted with an horizontal cyan line). Furthermore, it can be noted that Region II (yellow colored) follows the three sides of the $\lambda - \delta_0$ domain (δ_0 close to 1, small values of λ and δ_0 close to 0), Region III (highlighted in green) seems to embrace Region IV (highlighted in red) and Region V (highlighted in blue) is placed around $\delta_0 = \delta_0^* \simeq 0.2$ (see Sect. 2.4). By focusing the attention on a fixed value of stiffness ratio, e.g. $\lambda = 50$, which corresponds to a quite rigid obstacle (see the black vertical line in the map of Fig. 4), the occurrence of one scenario rather than the other depends on the value of the dimensionless gap δ_0. For this value of λ and for each identified region, representative PRCs of normalized excursion of absolute acceleration η_a (which allow to better highlight some behaviors, especially at low frequencies, compared to the PRCs of η_d) and corresponding to the colored squares, are arranged clockwise around the map. In these figures, the solid red curve refers to the forward sweep (indicated with an f in the legend), the dashed blue curve to the backward sweep (indicated with a b in the legend), the vertical arrows represents the jumps and the solid black horizontal line indicates the unit value of η_a. It can be observed that, starting from $\delta_0 = 1$ (see the figure on the top left), in which the situation is smooth, the encountered scenarios become gradually more complex decreasing δ_0 (move clockwise around the map, following the colored arrows), with the occurrence of the *primary resonance with right hysteresis* and different types of *secondary resonances* (with *right* or *left hysteresis* or of *non-regular* type), while in the limit case $\delta_0 = 0$ (bumpers initially in contact with the mass) the situation returns to be smooth, although the dynamics is different from that corresponding to $\delta_0 = 1$. Based on what was said in Sect. 2.4, the horizontal blue line $\delta_0 = \delta_0^*$, at the turn of which lies the Region V, represents the locus of the (λ, δ_0) pairs to which correspond two distinct roots of the Eq. (7), one of which (β_1) is equal to zero (Fig. 3(b)), regardless of the λ value. This line represents a watershed that divides the $\lambda - \delta_0$ plane into two parts. Above this line ($\delta_0^* \leq \delta_0 < 1$) there are the ($\lambda$, δ_0) pairs to which correspond two distinct roots (β_1 and β_2) of the Eq. (7); the two roots become coincident for $\delta_0 = 1$. PRCs do not highlight complex behaviors, except for some values of δ_0 (inside the Region IV); in these cases however, these complex behaviors are observed in small frequency ranges. More complex and varied scenarios are observed instead for $0 < \delta_0 < \delta_0^*$. In this zone there are the (λ, δ_0) pairs to which corresponds a single non-zero root (β_2) of the Eq. (7) and impact occurs immediately starting from $\beta = 0$. It is worth noting that inside Region VI very different behaviors can be observed, slightly varying δ_0, and the figure at the bottom left, corresponding to $\delta_0 = 0.1$, is just one example of one of these behaviors. From Fig. 4 it can be observed how, although the considered model (Fig. 1) seems apparently simple, by varying the involved parameters, even particularly complex scenarios can be encountered.

In the following Subsections, the seven identified scenarios will be described in more detail, starting from the analysis of the PRCs, and resorting to phase portraits in steady-state condition, Poincaré sections, basins of attraction and Fourier spectra.

3.1. Region I

For $\delta_0 \geq 1$ (Region I, horizontal orange line in Fig. 4), impact does not occur for any β value (Sect. 2.4). The corresponding PRCs of normalized excursion of relative displacement η_d, coincide with the thick black curve shown in Fig. 3(b), in which forward and backward curves overlap, without jumps or hysteresis. As concerns the PRC of excursion of absolute acceleration η_a (see the small figure on the top left corner of Fig. 4), it is very close to the PRC of η_d, due to the small value of ξ considered in the analyses. Both for displacement and for acceleration, as a consequence of the normalization adopted for the representation of the PRCs, the maximum value in resonance condition is equal to 1 and occurs for $\beta = \beta_{res} \simeq 0.99$. As concerns the eccentricity (e_d and e_a), it is null for each value of frequency ratio β.

3.2. Region II

For values of δ_0 inside Region II (highlighted in yellow in Fig. 4), PRCs are analogous to those shown in Fig. 5, which corresponds to $\delta_0 = 0.99$. In particular, both the PRCs of normalized excursion η_d (left vertical axis) and eccentricity e_d (right vertical axis) of relative displacement are depicted in Fig. 5(a), while both the PRCs of normalized excursion η_a (left vertical axis) and eccentricity e_a (right vertical axis) of absolute acceleration are depicted

in Fig. 5(b). It can be observed that forward (solid red lines) and backward (dashed blue lines) curves overlap, there are neither jumps nor hysteresis and the eccentricity (see the lower part of each figure) is equal to zero for each β value. Since in this Region $\delta_0^* < \delta_0 < 1$ and, in particular the selected value of δ_0 is very close to 1 (Sect. 2.4), impact occurs only in a small frequency range, in the neighbourhood of the resonant frequency, and it is highlighted by the presence of a spike in the PRC of η_a (Fig. 5(b)), while the peak of the PRC of η_d is slightly flattened (Fig. 5(a)), due to the presence of the obstacles, highlighted with an horizontal black line.

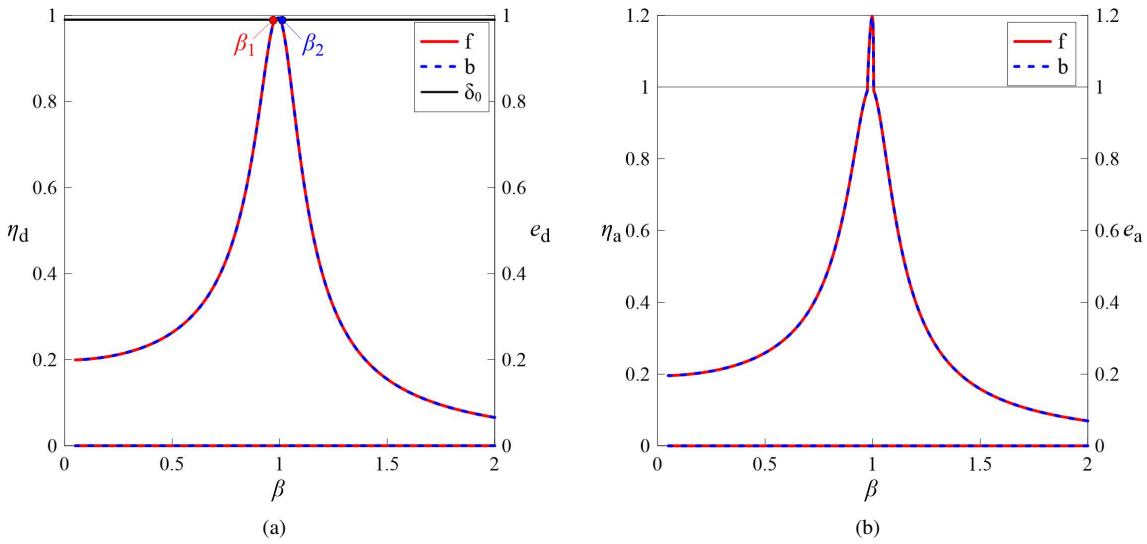

Figure 5: Region II ($\xi = 0.1$, $\gamma = 5$, $\lambda = 50$, $\delta_0 = 0.99$), forward (solid red line) and backward (dashed blue line) PRCs of: a) η_d and e_d (curves in the lower part of the graph); b) η_a and e_a (curves in the lower part of the graph). The vertical arrows represent the jumps.

In the frequency range associated with the occurrence of impact, between β_1 and β_2 (see the red and blue dots in Fig. 5(a)), there is only a periodic steady-state solution (Fig. 6(a)), with the same period of the excitation (thus $n = T_s/T_f = 1$, where T_s is the period of the solution and T_f is the forcing period, as it can be seen from Fig. 6(b), where only the fundamental harmonic is observed.

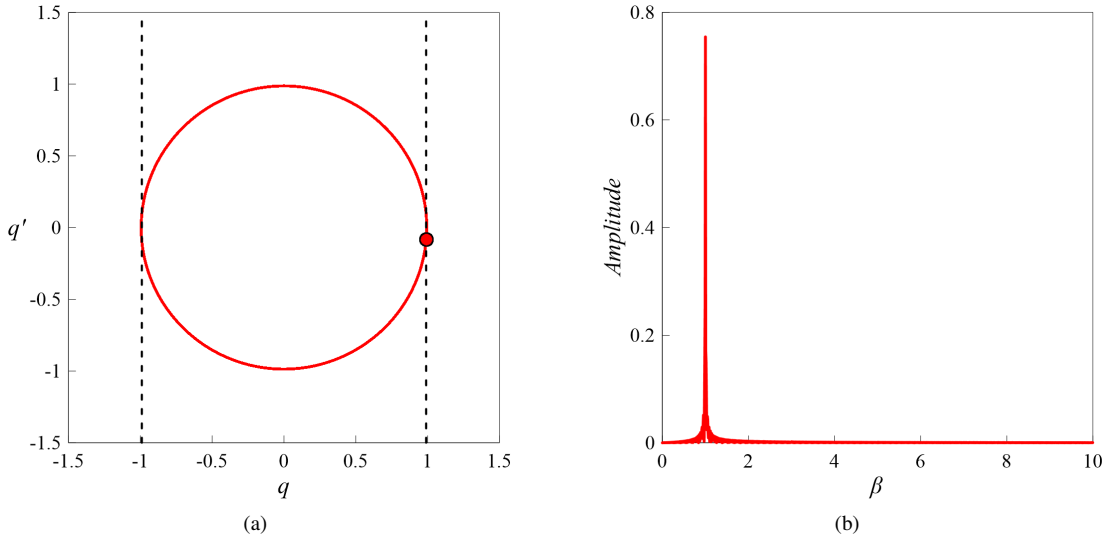

Figure 6: Region II ($\xi = 0.1$, $\gamma = 5$, $\lambda = 50$, $\delta_0 = 0.99$): a) phase portrait with Poincaré section and b) Fourier spectrum for $\beta = 1$.

Consequently, in the Poincaré section, obtained by marking the trajectory at times that are integer multiples of the forcing period T_f, the points coincide with the single point represented by a red dot in Fig. 6(a). At steady-state, reached with a small number of forcing cycles, the limit cycle in the phase plane is similar to a circle, slightly flattened at the ends, due to the impact and, in each forcing cycle, the mass hits each bumper (two vertical dashed black lines) once.

3.3. Region III (upper part)

In the green portion of the $\lambda - \delta_0$ plane (Region III), just below the yellow one (Region II, Fig. 4), from Fig. 7, which refers to $\delta_0 = 0.8$, it can be observed that, compared to the previous case (Fig. 5), the frequency range characterized by the occurrence of impact is greater. Furthermore, the jump phenomena (highlighted with vertical arrows) and the *primary resonance with right hysteresis* are observed. Also in this case, eccentricity is zero for each value of β.

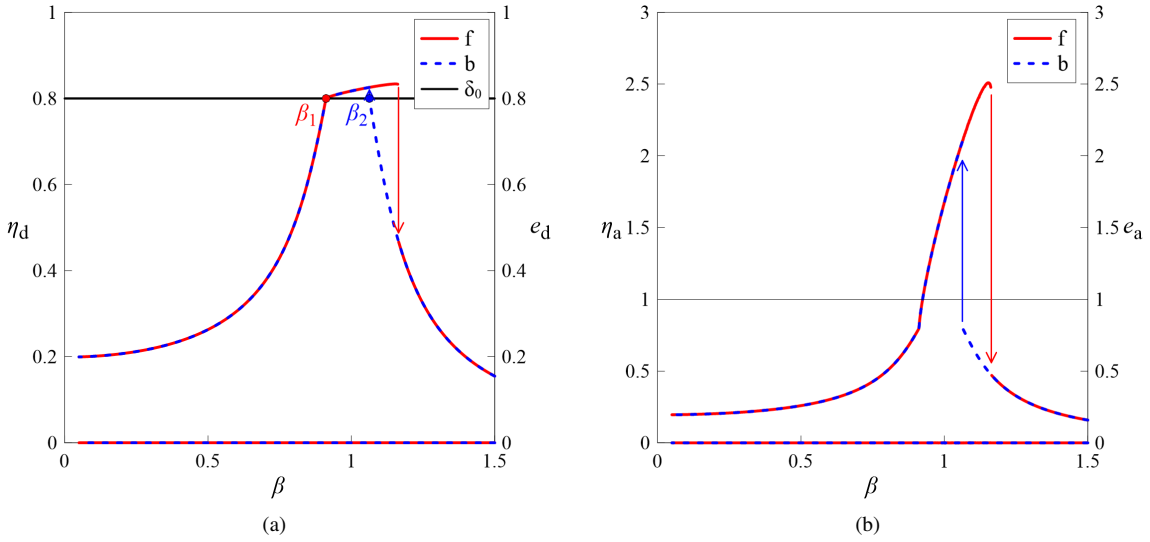

Figure 7: Region III, upper part ($\xi = 0.1$, $\gamma = 5$, $\lambda = 50$, $\delta_0 = 0.8$), forward (solid red line) and backward (dashed blue line) PRCs of: a) η_d and e_d (curves in the lower part of the graph); b) η_a and e_a (curves in the lower part of the graph). The vertical arrows represent the jumps.

In the frequency range between the two jumps (e.g. $\beta = 1.1$), there are two steady-state solutions (Fig. 8(a)):

- Large-amplitude resonant motion with impact (red curve);
- Small-amplitude non-resonant motion without impact (blue curve).

Actually, there would be also an unstable solution, that could not be obtained with the used procedure. Both the observed solutions are periodic, with the same period of the excitation ($n = 1$). Consequently, in both cases, at steady-state (reached with a small number of forcing cycles), the points in the Poincaré sections coincide with a single point, colored red for the large-amplitude motion and colored blue for the small-amplitude motion. In the Fourier spectra (Fig. 8(c) and (d)), only the fundamental harmonic component is observed. From Fig. 8(a) it can be observed that the small-amplitude limit cycle is similar to a circle, while the limit cycle of the large-amplitude motion is slightly flattened at the ends, due to the occurrence of impact, and in each forcing cycle, the mass hits each bumper once. The basins of attraction of the two solutions are shown in Fig. 8(b), together with the initial conditions for the sine sweep frequency sub-range that includes the value $\beta = 1.1$, obtained with the continuation technique during the forward (yellow right-pointing triangle) and the backward (yellow left-pointing triangle) sweep. The basins were obtained considering a sufficiently dense mesh of initial conditions (q_0, q_0'), represented with colored dots. Each basin is made up of the set of dots (initial conditions) that lead to the corresponding attractor. In particular, red dots represent the set of initial conditions that lead to the large-amplitude motion, while blue dots represent the set of initial conditions that

lead to the small-amplitude motion. It can be observed that the shape of the basins is smooth and regular, due to the periodic behavior of the system.

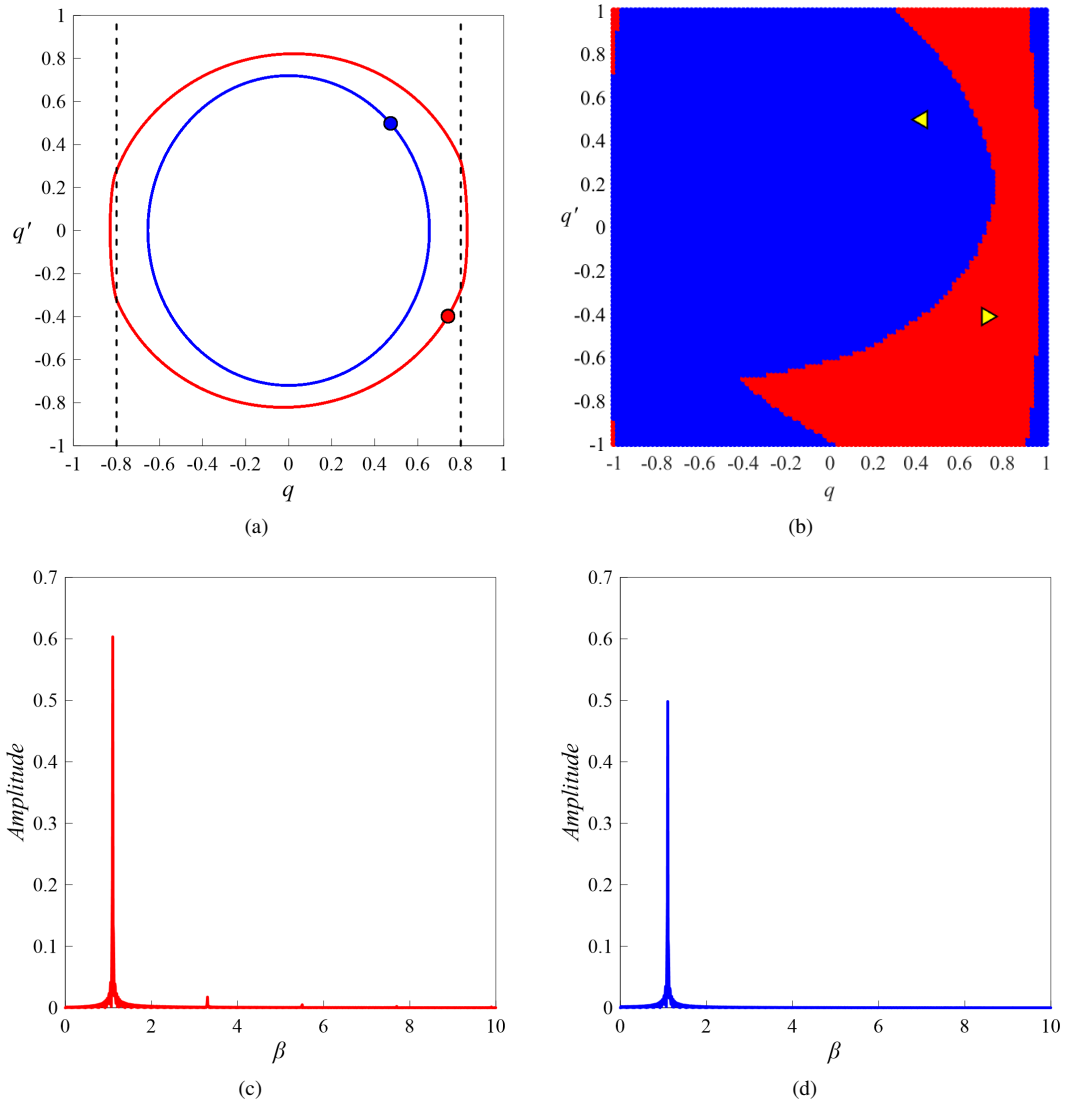

Figure 8: Region III, upper part ($\xi = 0.1$, $\gamma = 5$, $\lambda = 50$, $\delta_0 = 0.8$, $\beta = 1.1$): a) phase portraits with Poincaré sections; b) basins of attraction; Fourier spectra: c) ($q_0 = 0.74$, $q_0' = -0.4$), yellow right-pointing triangle; d) ($q_0 = 0.47$, $q_0' = 0.5$), yellow left-pointing triangle.

3.4. Region IV

Decreasing the dimensionless gap δ_0 and entering Region IV, in the PRCs (Fig. 9, which corresponds to $\delta_0 = 0.4$), in addition to the *primary resonance with right hysteresis*, the presence of a *secondary resonance* is observed (zoomed rectangular area). This secondary resonance is characterized by the occurrence of a *right hysteresis*, with zero eccentricity, followed by a small frequency range characterized by increasing excursion and zero eccentricity. After an abrupt reduction of excursion, a section, in the neighbourhood of $\beta \simeq 0.8$, with eccentricity other than zero and characterized by an almost constant value of excursion, is observed. The secondary resonance occurs at the frequency value for which, at steady-state, the mass just begins to touch the bumpers with a velocity close to zero ($\beta = \beta_1 \simeq 0.72$, Sect. 2.4, highlighted with a red dot in Fig. 9(a)).

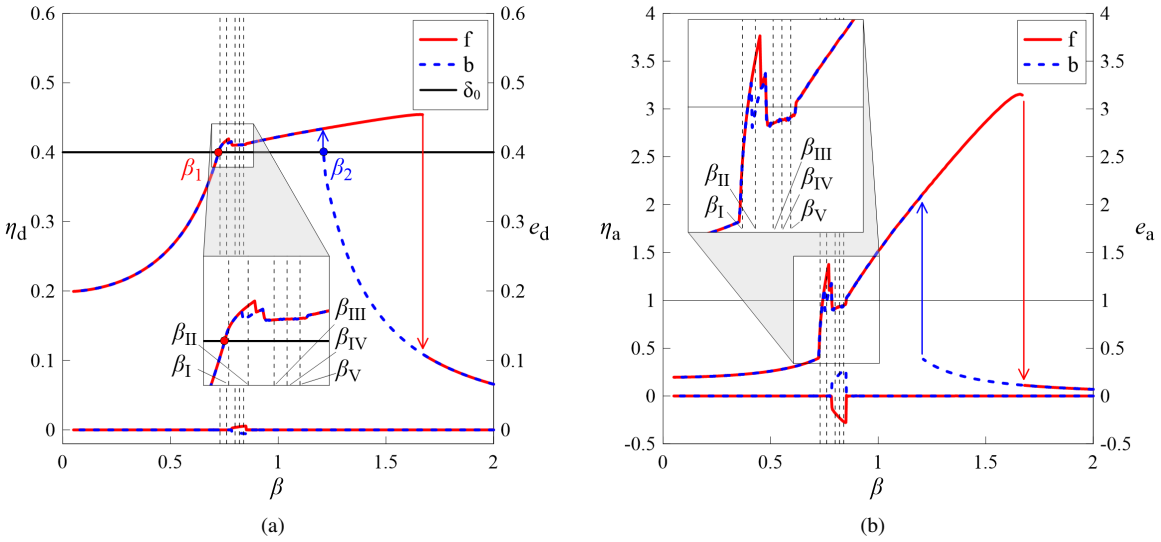

Figure 9: Region IV ($\xi = 0.1$, $\gamma = 5$, $\lambda = 50$, $\delta_0 = 0.4$), forward (solid red line) and backward (dashed blue line) PRCs of: a) η_d and e_d (curves in the lower part of the graph); b) η_a and e_a (curves in the lower part of the graph). The vertical arrows represent the jumps. A detail of the secondary resonance is shown in the rectangular zoomed area. The dashed vertical lines represent β values that will be investigated in more detail.

This causes the transition from a single periodic non-impacting steady-state solution, to a single impacting periodic multi-frequency steady-state solution (see Fig. 10(a), corresponding to $\beta = \beta_I = 0.73$, first vertical dashed line in Fig. 9). In the following, this condition will be referred to as *primary grazing*, because it occurs when the periodic non-impacting limit cycle, expanding as β increases, begins to touch the obstacles, with a velocity close to zero.

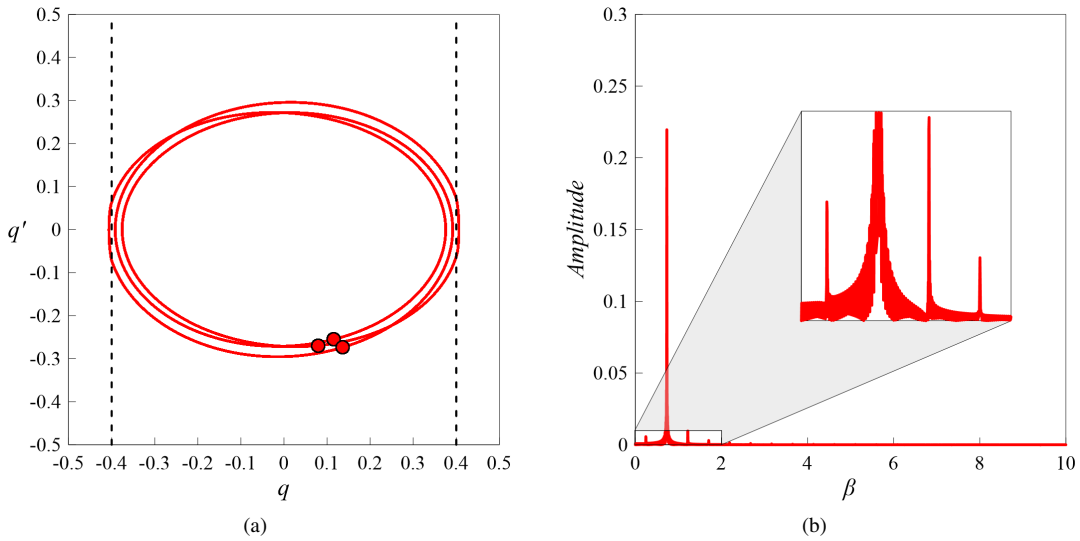

Figure 10: Region IV ($\xi = 0.1$, $\gamma = 5$, $\lambda = 50$, $\delta_0 = 0.40$): a) phase portrait with Poincaré section and b) Fourier spectrum for $\beta = \beta_I$.

At steady-state, reached with a quite small number of forcing cycles, the attractor is characterized by interweaving cycles, very close to each other, with antisymmetric envelope (Fig. 10(a)) and has a period that is three times the forcing period ($n = 3$). Consequently, in the Poincaré section, three points were observed. In the Fourier spectrum (Fig. 10(b)), in addition to the fundamental frequency, it is also possible to observe the other commensurate frequencies, characterized by a much smaller amplitude, one of which is equal to one third of the fundamental. At steady-state,

the mass alternatively hits once only one of the two bumpers, then neither, then only the other. In the frequency range characterized by the presence of the *secondary right hysteresis* ($\beta = \beta_{II} = 0.76$, second vertical dashed line in Fig. 9) two coexisting solutions, each with antisymmetric envelope, were observed (Fig. 11(a)):

- A periodic multi-frequency solution (red curve), with $n = 3$, associated with the forward sweep;
- A quasi-periodic solution (blue curve), associated with the backward sweep.

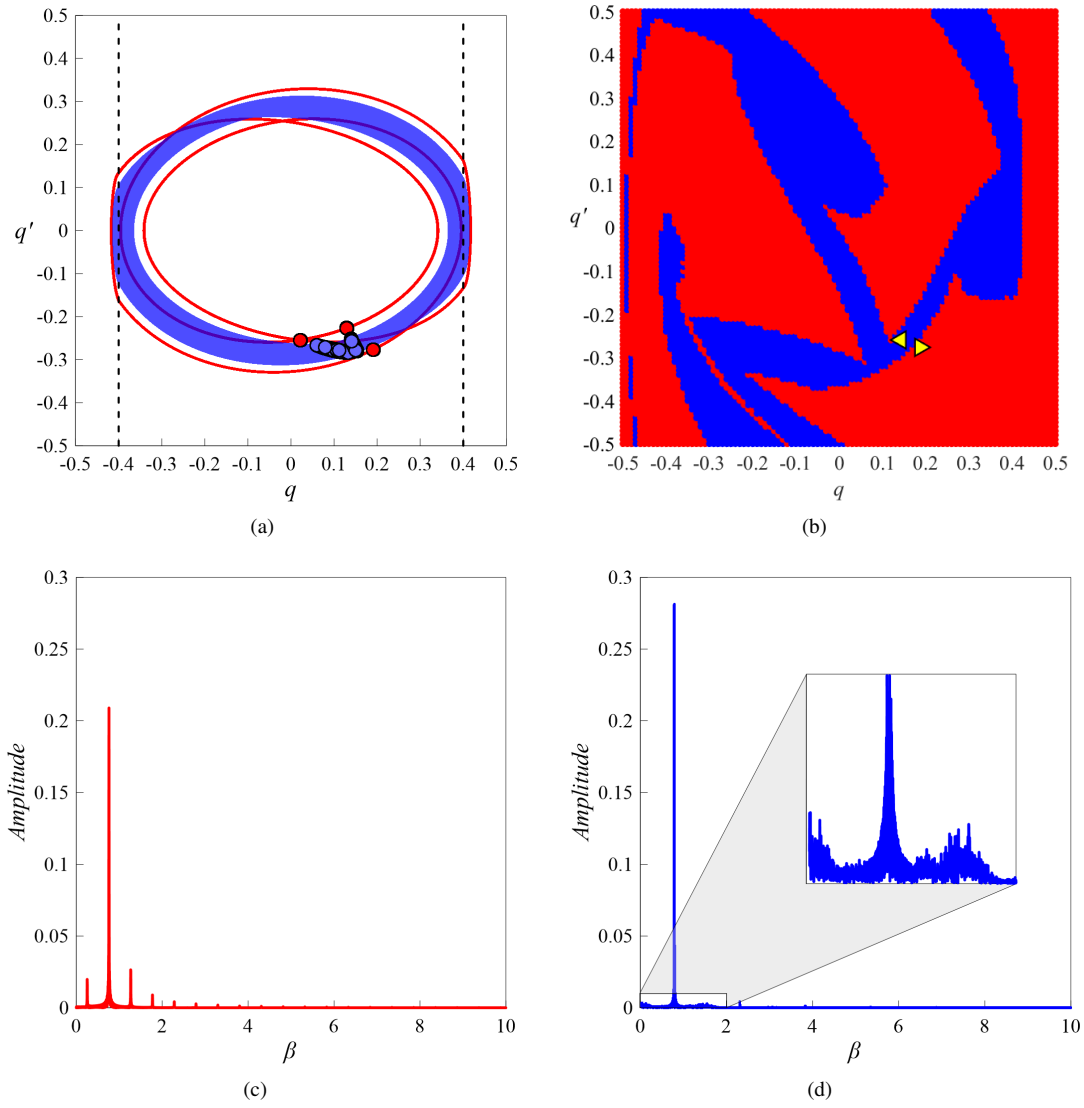

Figure 11: Region IV ($\xi = 0.1$, $\gamma = 5$, $\lambda = 50$, $\delta_0 = 0.4$, $\beta = \beta_{II}$): a) phase portraits with Poincaré sections; b) basins of attraction; Fourier spectra: c) ($q_0 = 0.19$, $q_0' = -0.28$), yellow right-pointing triangle; d) ($q_0 = 0.14$, $q_0' = -0.26$), yellow left-pointing triangle.

Compared to the *primary right hysteresis* (Fig. 8(a)), both solutions are associated with the occurrence of impact and one of them is quasi-periodic (blue curve). As regards the periodic solution (red curve), which is similar to the limit cycle shown in Fig. 10(a), the considerations made previously apply. The differences concern the amplitude of the limit cycle, the relative position of the interweaving cycles, which lead to a different distance between the three points in the Poincaré section, and a greater amplitude of the harmonic components in the Fourier spectrum (Fig. 11(c)). The limit cycle corresponding to the quasi-periodic solution (blue curve) is quite thick and it is characterized by a more

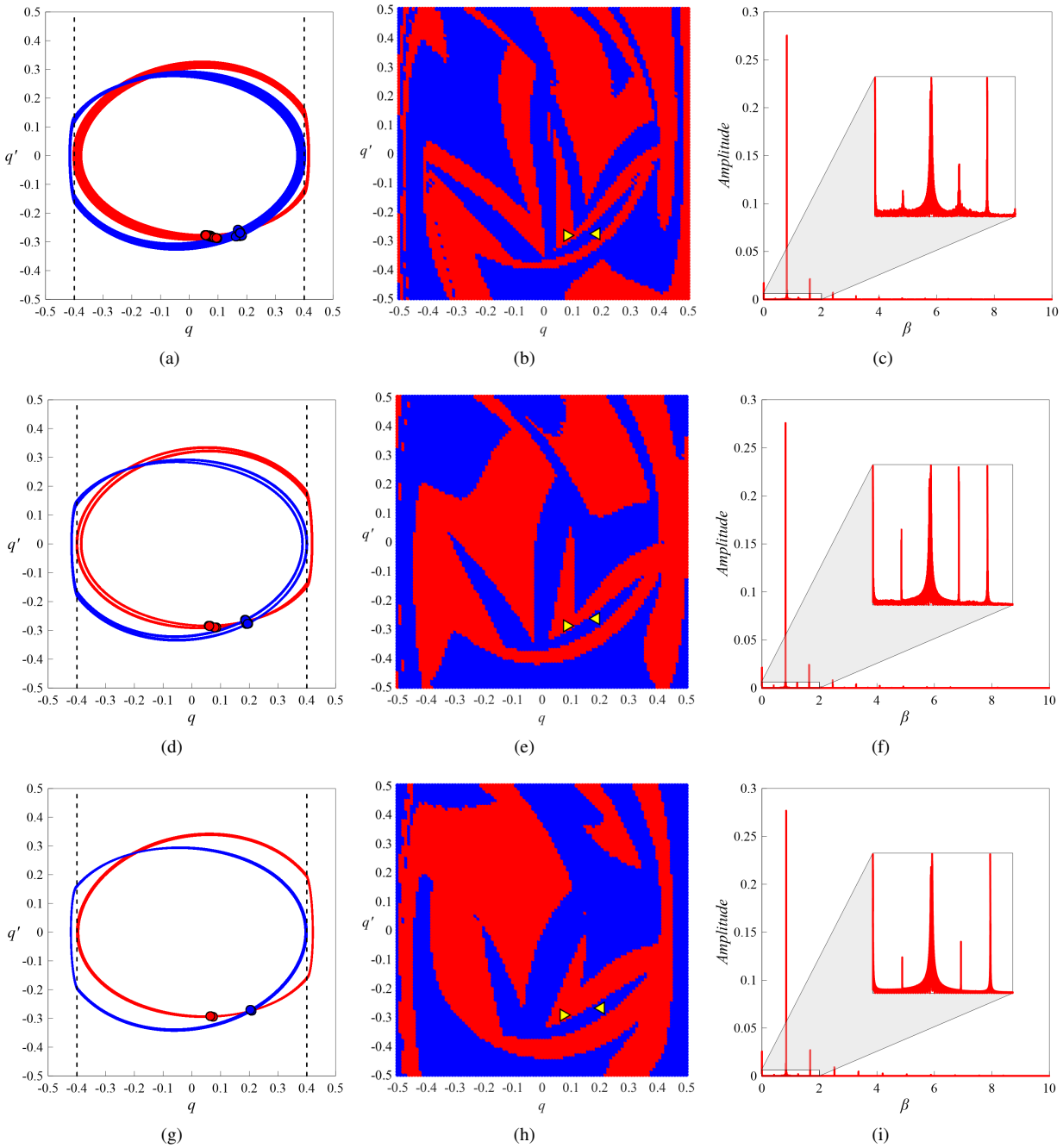

Figure 12: Region IV ($\xi = 0.1$, $\gamma = 5$, $\lambda = 50$, $\delta_0 = 0.4$), phase portraits with Poincaré sections for: a) $\beta = \beta_{\mathrm{III}}$; d) $\beta = \beta_{\mathrm{IV}}$; g) $\beta = \beta_{\mathrm{V}}$; basins of attraction for: b) $\beta = \beta_{\mathrm{III}}$; e) $\beta = \beta_{\mathrm{IV}}$; h) $\beta = \beta_{\mathrm{V}}$; Fourier spectra for: c) $\beta = \beta_{\mathrm{III}}$; f) $\beta = \beta_{\mathrm{IV}}$; i) $\beta = \beta_{\mathrm{V}}$.

complex structure of the Poincaré section. In the Fourier spectrum (Fig. 11(d)), the fundamental frequency stands out significantly compared to the others incommensurate frequencies, which can be seen better in the rectangular zoomed area. Given the quasi-periodic nature of the response, even considering a high number of forcing cycles, it is not possible to reach a real stationary condition; this is reflected in the number of impacts per forcing cycle, which is not constant but changes as time goes by. The basins of attraction of the two coexisting solutions are shown in Fig. 11(b), together with the initial conditions for the sine sweep frequency sub-range that includes the value $\beta = \beta_{\mathrm{II}}$, obtained with the continuation technique during the forward (yellow right-pointing triangle) and the backward (yellow left-pointing triangle) sweep. Compared to Fig. 8(b), the shape of the basins, especially that of the basin of attraction of the quasi-periodic attractor (highlighed in blue), is less regular. The secondary downward jump in the forward sweep occurs when one of the internal interweaving cycles grazes the obstacles. In the following, this condition will be referred to as *secondary grazing*, because it occurs when, in addition to the primary orbit, which impacts the obstacles evidently, one of the internal cycles or loops, expanding, begins to touch them, with a velocity close to zero. This causes the sudden transition, during the forward sweep, to a quasi-periodic attractor, analogous to the blue one shown in Fig. 11(a). This single quasi-periodic solution was observed in the frequency range, after the jump, characterized by increasing excursion and zero eccentricity, followed by an abrupt reduction of excursion. In the subsequent frequency range, characterized by eccentricity other than zero and almost constant excursion, the existence of a *pair of quasi-periodic solutions* is observed (Fig. 12(a), which corresponds to $\beta = \beta_{\mathrm{III}} = 0.80$, third vertical dashed line in Fig. 9). These two limit cycles have the same frequency content, the same excursion but are characterized by eccentricities, equal in absolute value but with opposite sign. Consequently, the two solutions are not antisymmetric in themselves, but the antisymmetry is achieved through their envelope. Compared to the quasi-periodic solution shown in Fig. 11(a), the limit cycles that make up the pair are weakly quasi-periodic (less thick limit). Consequently, the incommensurate frequencies are much less obvious (Fig. 12(c)). By focusing the attention on the single cycle that makes up the pair, it can be noted that, the mass impacts one of the two bumpers in an evident manner, while it grazes the other slightly. The basins of attraction of the two solutions are shown in Fig. 12(b) and are characterized by quite irregular boundaries. By increasing β, on the one hand the extent of the impact gradually increases, on the other the grazing reduces (see Fig. 11(d), corresponding to $\beta = \beta_{\mathrm{IV}} = 0.82$ and Fig. 11(g), corresponding to $\beta = \beta_{\mathrm{V}} = 0.84$). Consequently, the quasi-periodicity of the solutions, and thus the irregularity of the basins of attraction, decrease. Furthermore, as the quasi-periodicity decreases, the number of forcing cycles required to reach the stationary is also reduced. After this range, characterized by irregular behavior, and before the *primary right hysteresis*, a single periodic steady-state solution with $n = 1$ is observed. As concerns the *primary right hysteresis*, in the frequency range between the two jumps, everything goes as described in Sect. 3.3.

3.5. Region III (lower part)

From Fig. 4 it was observed that Region III (highlighted in green) embraces Region IV (highlighted in red). Starting from Region IV and moving into the lower green band, by decreasing δ_0, from Fig. 13, which refers to $\delta_0 = 0.25$, it can be observed that the PRCs are qualitatively similar to those observed for $\delta_0 = 0.8$ (Fig. 7) and are characterized by the presence of only the *primary resonance with right hysteresis* and by a null eccentricity for each β value. Compared to the case $\delta_0 = 0.8$, the frequency range associated with the occurrence of impact is larger, the primary hysteresis is shifted to higher frequency values and its extension is greater. Furthermore, for $\beta = \beta_1 = 0.4575$, highlighted with a red dot in Fig. 13(a), it can be observed that, in the PRCs, especially that of η_{a}, a rather vertical section is observed. When the mass reaches the obstacles, a distortion of the limit cycle occurs, which gradually assumes the appearance of the red one shown in the Fig. 14(a) characterized by an evident antisymmetry. As previously said in Sect. 3.3, in the frequency range between the two jumps (e.g. $\beta = 2$), two steady-state solutions (Fig. 14(a)), a large-amplitude resonant motion with impact (red curve) and a small-amplitude non-resonant motion without impact (blue curve), are observed. Both solutions are periodic, with the same period of the excitation ($n = 1$). Compared to the case $\delta_0 = 0.8$ (Fig. 8), as previously said, the large amplitude limit-cycle turns out to be more distorted and in the corresponding Fourier spectrum, in addition to the fundamental harmonic, the presence of another harmonic component, with smaller amplitude, at a frequency that is three times that of the fundamental, is also observed, (Fig. 15(a)) whereas in the Fourier spectrum corresponding to the small-amplitude motion, only the fundamental harmonic component is observed (Fig. 15(b)). Furthermore, since δ_0 is lower, that is the bumpers are closer to the mass, the large-amplitude limit cycle (red curve in Fig. 14(a)) is more squashed at the

ends, due to the occurrence of impact, and in each forcing cycle, the mass hits each bumper once. As concerns the small-amplitude limit cycle, it is more like an ellipse.

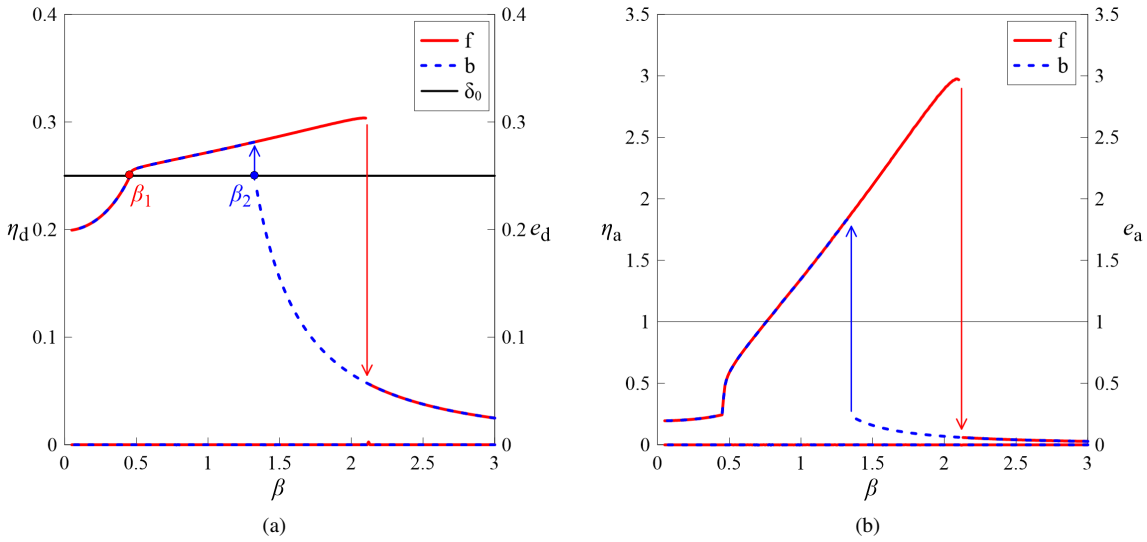

Figure 13: Region III, lower part ($\xi = 0.1$, $\gamma = 5$, $\lambda = 50$, $\delta_0 = 0.25$), forward (solid red line) and backward (dashed blue line) PRCs of: a) η_d and e_d (curves in the lower part of the graph); b) η_a and e_a (curves in the lower part of the graph). The vertical arrows represent the jumps.

The basins of attraction of the two solutions are shown in Fig. 14(b), together with the initial conditions for the sine sweep frequency sub-range including the value $\beta = 2$, obtained with the continuation technique during the forward (yellow right-pointing triangle) and the backward (yellow left-pointing triangle) sweep. As in the case $\delta_0 = 0.8$ (Fig. 8(b)), also in this case the shape of the basins returns to be smooth and regular.

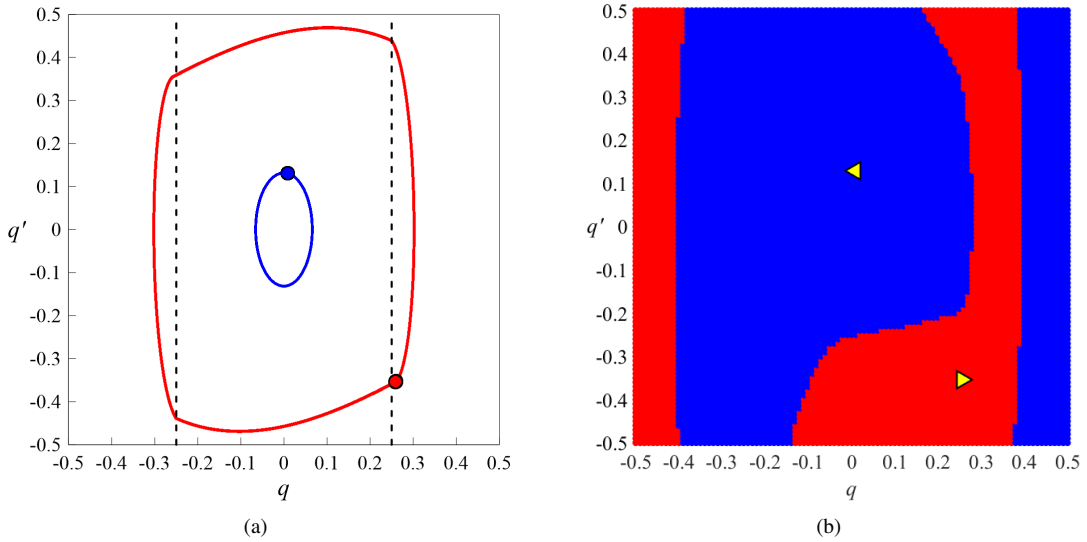

Figure 14: Region III, lower part ($\xi = 0.1$, $\gamma = 5$, $\lambda = 50$, $\delta_0 = 0.25$): a) phase portraits with Poincaré sections and b) basins of attraction for $\beta = 2$.

3.6. Region V

The scenarios previously analyzed referred to values of dimensionless gap $\delta_0^* < \delta_0 \leq 1$, for which Eq. (7) admits two non-zero roots (β_1 and β_2, coincident for $\delta_0 = 1$). Moving into the blue region, which straddles the

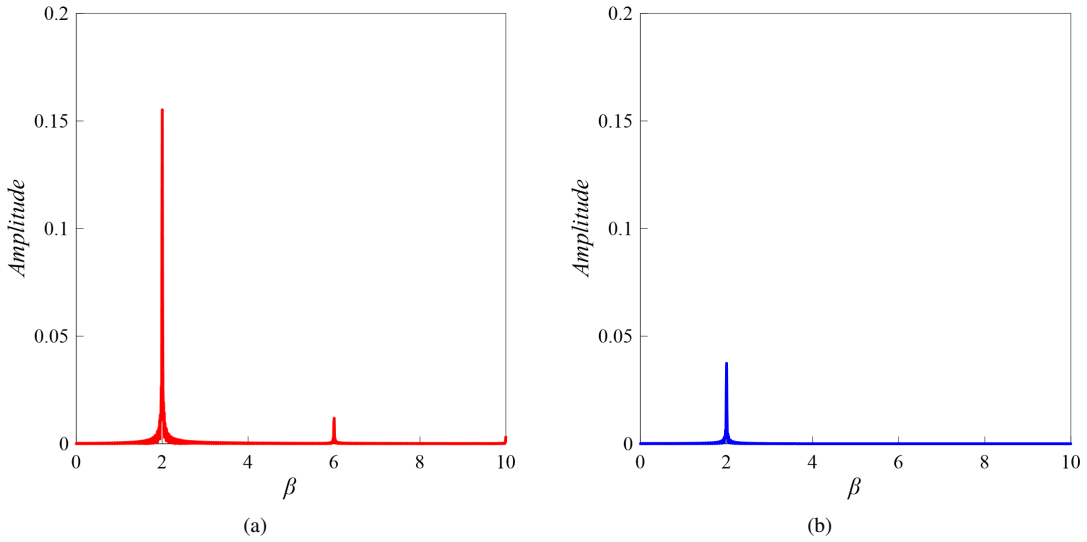

Figure 15: Region III, lower part ($\xi = 0.1$, $\gamma = 5$, $\lambda = 50$, $\delta_0 = 0.25$): a) Fourier spectra for $\beta = 2$ and initial conditions: c) ($q_0 = 0.26$, $q_0' = -0.35$); d) ($q_0 = 0.008$, $q_0' = 0.13$).

line $\delta_0 = \delta_0^* \simeq 0.2$, in the forward sweep impact occurs immediately starting from $\beta = \beta_1 = 0$ and the PRCs are characterized by the presence of both the *primary resonance with right hysteresis* and several *secondary resonances without hysteresis* in the low frequency range (enclosed within an ellipse in Fig. 16). A detail of the smaller resonances is shown in the rectangular zoomed area.

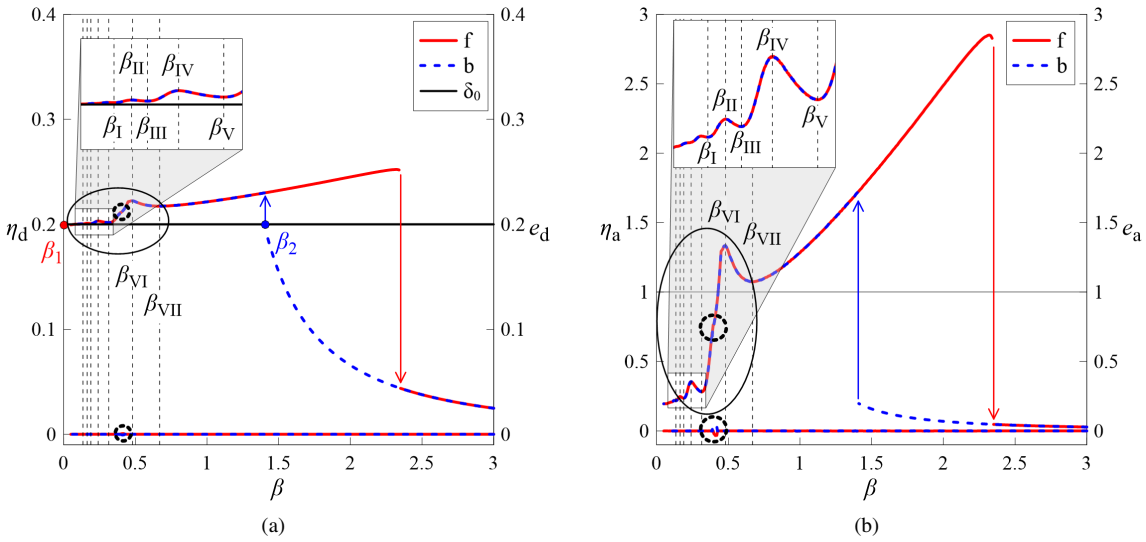

Figure 16: Region V ($\xi = 0.1$, $\gamma = 5$, $\lambda = 50$, $\delta_0 = \delta_0^*$), forward (solid red line) and backward (dashed blue line) PRCs of: a) η_d and e_d (curves in the lower part of the graph); b) η_a and e_a (curves in the lower part of the graph). The vertical arrows represent the jumps. The secondary resonances are enclosed by the solid black ellipse and a detail of the smaller resonances is shown in the rectangular zoomed area. The small dashed black circles highlight the small frequency interval characterized by non-zero eccentricity. The dashed vertical lines represent β values that will be investigated in more detail.

It can be observed that eccentricity is always zero except for a very small frequency range in the neighbourhood of $\beta \simeq 0.4$ (highlighted with a small dashed circle). In the low frequency range, characterized by the alternation of ridges and valleys, a single periodic multi-frequency solution, with $n = 1$ is observed.

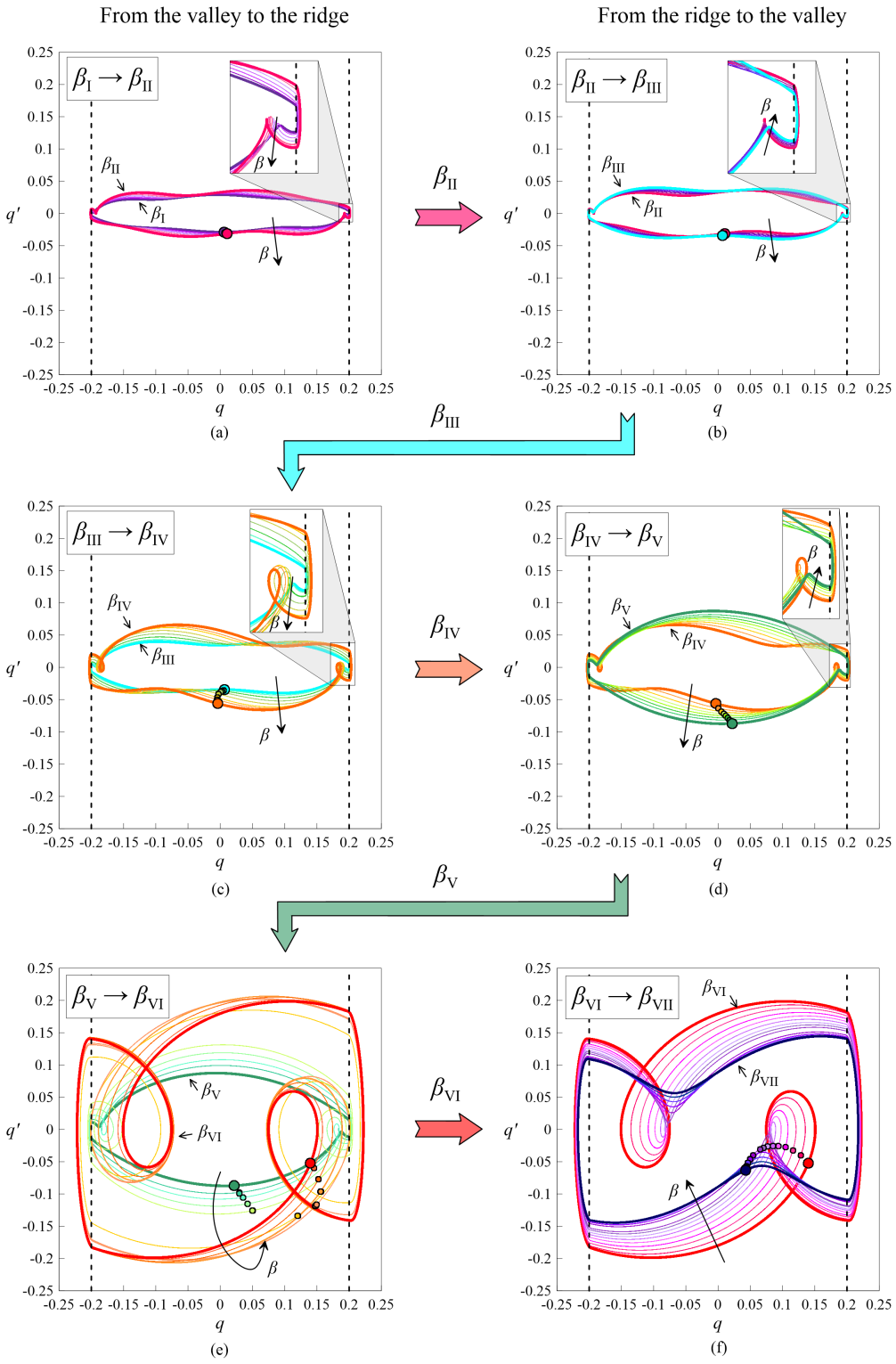

Figure 17: Region V ($\xi = 0.1$, $\gamma = 5$, $\lambda = 50$, $\delta_0 = \delta_0^*$), secondary resonances in the low frequency range: evolution of the phase portraits passing from the valley to the ridge (left column) and passing from the ridge to the valley (right column): a) $\beta_{\rm I} \rightarrow \beta_{\rm II}$; b) $\beta_{\rm II} \rightarrow \beta_{\rm III}$; c) $\beta_{\rm III} \rightarrow \beta_{\rm IV}$; d) $\beta_{\rm IV} \rightarrow \beta_{\rm V}$; e) $\beta_{\rm V} \rightarrow \beta_{\rm VI}$; f) $\beta_{\rm VI} \rightarrow \beta_{\rm VII}$. The cycle corresponding to the investigated valleys and ridges are represented with thicker lines. The order of the sub-figures is given by the colored arrows.

In Fig. 17, each sub-figure describes the evolution of the phase portraits, at steady-state, moving from one valley to the next ridge (left column, Fig. 17(a), (c) and (e)) and moving from one ridge to the next valley (right column, Fig. 17(b), (d) and (f)). The β values corresponding to the investigated ridges and valleys are indicated with Roman numerals in Fig. 16 and the associated phase portraits are represented with thicker lines. From Fig. 17 it can be observed that, starting from a valley ($\beta_{\mathrm{I}} = 0.192, \beta_{\mathrm{III}} = 0.316$ or $\beta_{\mathrm{V}} = 0.48$) and approaching the next ridge ($\beta_{\mathrm{II}} = 0.24$, Fig. 17(a), $\beta_{\mathrm{IV}} = 0.43$, Fig. 17(c), or $\beta_{\mathrm{V}} = 0.67$, Fig. 17(e)), in the phase portrait two internal loops appear. These loops were not observed for $\beta < \beta_{\mathrm{I}}$. As β increases, the internal loops gradually move inward, growing first and then getting smaller. Referring to the two smaller considered ridges (Fig. 17(a) and (c)), they never touch the obstacles; consequently, in each forcing cycle, the mass hits each bumper once. As regards the larger ridge (Fig. 17(e)) instead, it is observed that the internal loops come to touch the obstacles (*secondary grazing*), more or less in the middle of the ascending branch, just before the frequency range with non-zero eccentricity. This will be investigated in more detail later.

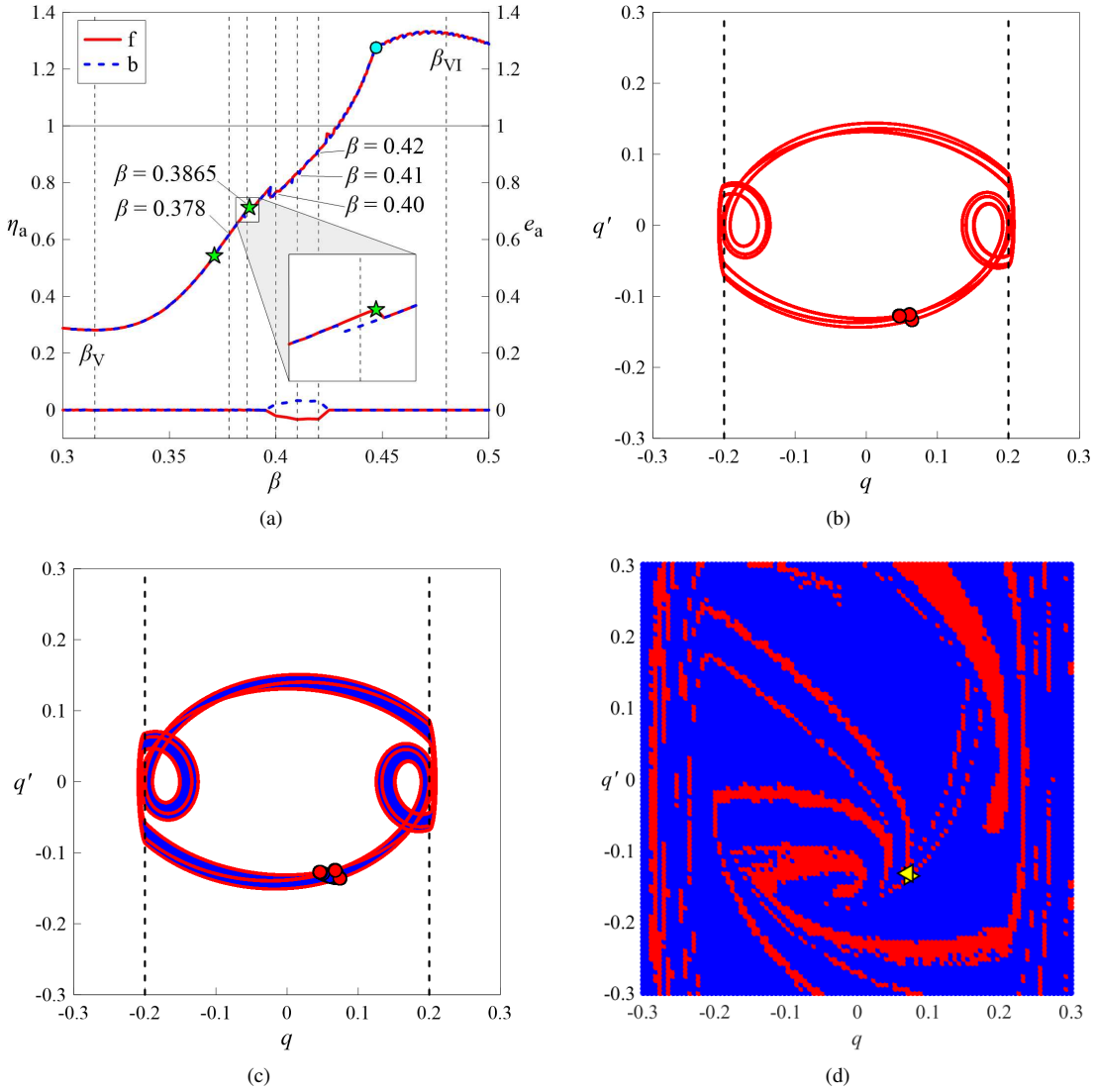

Figure 18: Region V ($\xi = 0.1$, $\gamma = 5$, $\lambda = 50$, $\delta_0 = \delta_0^*$): a) zoom of the PRCs of η_{a} and e_{a} in the neighbourhood of the frequency range with non-zero eccentricity; phase portraits with Poincaré sections for: b) $\beta = 0.378$; c) $\beta = 0.3865$ (right hysteresis) d) basins of attraction for $\beta = 0.3865$ (right hysteresis).

Beyond the frequency range with non-zero eccentricity, a single periodic solution with $n = 1$ is observed again. The two internal loops touch the obstacles, causing the mass to impact each bumper twice for each forcing cycle. Subsequently, by further increasing β, the loops begin to move inward, becoming gradually smaller (Fig. 17(e)) and when they no longer intersect the obstacles, the mass returns to hits each bumper once. Conversely, starting from a ridge (β_{II}, β_{IV} or β_{VI}) and approaching the next valley (β_{III}, Fig. 17(b), β_{V}, Fig. 17(d), or β_{VII}, Fig. 17(f)), the two internal loops gradually disappear, taking on the appearance of cusps progressively more rounded and in each forcing cycle, the mass hits each bumper once. Let's now focus the attention on the frequency range enclosed by the small dashed circle, more or less in the middle of the ascending branch, just before the frequency range with non-zero eccentricity. When the internal loops reach the obstacles (*secondary grazing*, indicated by the first green star on the left in Fig. 18(a)), the transition from a periodic impacting steady-state solution with $n = 1$, to a periodic impacting steady-state solution with $n = 3$ is observed (Fig. 18(b)), in a similar way to what was seen for $\delta_0 = 0.4$. At steady-state, reached with a quite small number of forcing cycles, the solution is similar to the one shown in Fig. 10(a); in addition to the interweaving cycles there are also six internal loops, two of which intersect the obstacles. Consequently, in each forcing cycle, the mass impacts in one cycle once a bumper and two times the other, in the next cycle once both, and so on alternately. As also observed for $\delta_0 = 0.4$ (Fig. 11), a small frequency range characterized by the presence of a *secondary right hysteresis* with zero eccentricity follows (see the zoomed area in Fig. 18(a)). In order to highlight this hysteresis a quite small frequency increment and a higher number of forcing cycles were required. At the hysteresis two coexisting solutions, both associated with the occurrence of impact and each with antisymmetric envelope, were observed (Fig. 18(c)):

- A periodic multi-frequency solution (red curve), with $n = 3$, similar to the limit cycle shown in Fig. 18(a) and associated with the forward sweep;
- A quasi-periodic solution (blue curve), associated with the backward sweep.

The basins of attraction of the two coexisting solutions are shown in Fig. 18(d). It can be observed that the boundaries of the basins are quite irregular (fractal) and most of the initial conditions lead to the quasi-periodic solution (blue basin). In the forward sweep a sudden small downward jump was observed, when two of the internal loops of the solution (see Fig. 18(b), or the red curve in Fig. 18(c)) reach the obstacles (another *secondary grazing*, indicated by the second green star in Fig. 18(a))), causing the transition to a quasi-periodic attractor, similar to the blue one shown in Fig. 18(c). After another small jump, a small frequency interval, in the neighbourhood of $\beta \simeq 0.4$, with non-zero eccentricity follows. In this frequency range, a *pair of quasi-periodic solutions*, whose overall envelope is antisymmetric, is observed (Fig. 19(a), which corresponds to $\beta = 0.40$). Each of the cycles that make up the pair have internal loops, which, as time goes by, approach, cross and then move away from the vertical dashed lines representing the position of the obstacles. In particular, by focusing the attention on the single cycle that makes up the pair, it can be observed that, one of the internal loop impacts one bumper in an evident manner, while the other only grazes the other bumper. This results, for each of the two solutions, in a different number of impacts, in each forcing cycle, to the right and left as time goes on. It is worth noting that, to reach a stationary condition, a high number of cycles was required. Since the limit cycles that make up the pair are weakly quasi-periodic, the incommensurate frequencies are not very evident in the Fourier spectrum (Fig. 19(c)). The basins of attraction of the two solutions are shown in Fig. 19(b) and are characterized by quite irregular (fractal) boundaries. By increasing β (Fig. 19(d), which corresponds to $\beta = 0.41$ and Fig. 19(i), which corresponds to $\beta = 0.42$), on the one hand the extent of the impact gradually increases, on the other the grazing reduces and therefore also the quasi-periodicity and the complexity of the basins of attraction. As previously said, after the frequency range with non-zero eccentricity and before the ridge (β_{VI}), a single periodic solution, with $n = 1$, is observed again, in which the inner loops, that initially intersect both the obstacles (double impact), progressively become smaller and move inward as β increases. When they no longer intersect the obstacles (cyan dot in Fig. 18(a)), the mass returns to hits each bumper once. This sequence of behaviors, similar to that observed for $\delta_0 = 0.4$ and related to the occurrence of consecutive *secondary grazing*, was not observed before the other smaller ridges, where the internal loops do not cause further impacts, but evolve far from the obstacles, as β varies.

3.7. Region VI

Further reducing the dimensionless gap δ_0, we move onto Region VI (highlighted in magenta in Fig. 4). Since $0 < \delta_0 < \delta_0^*$, Eq. 7 admits only a non-zero root (β_2, see Sect. 2.4) and impact occurs already starting from $\beta = 0$.

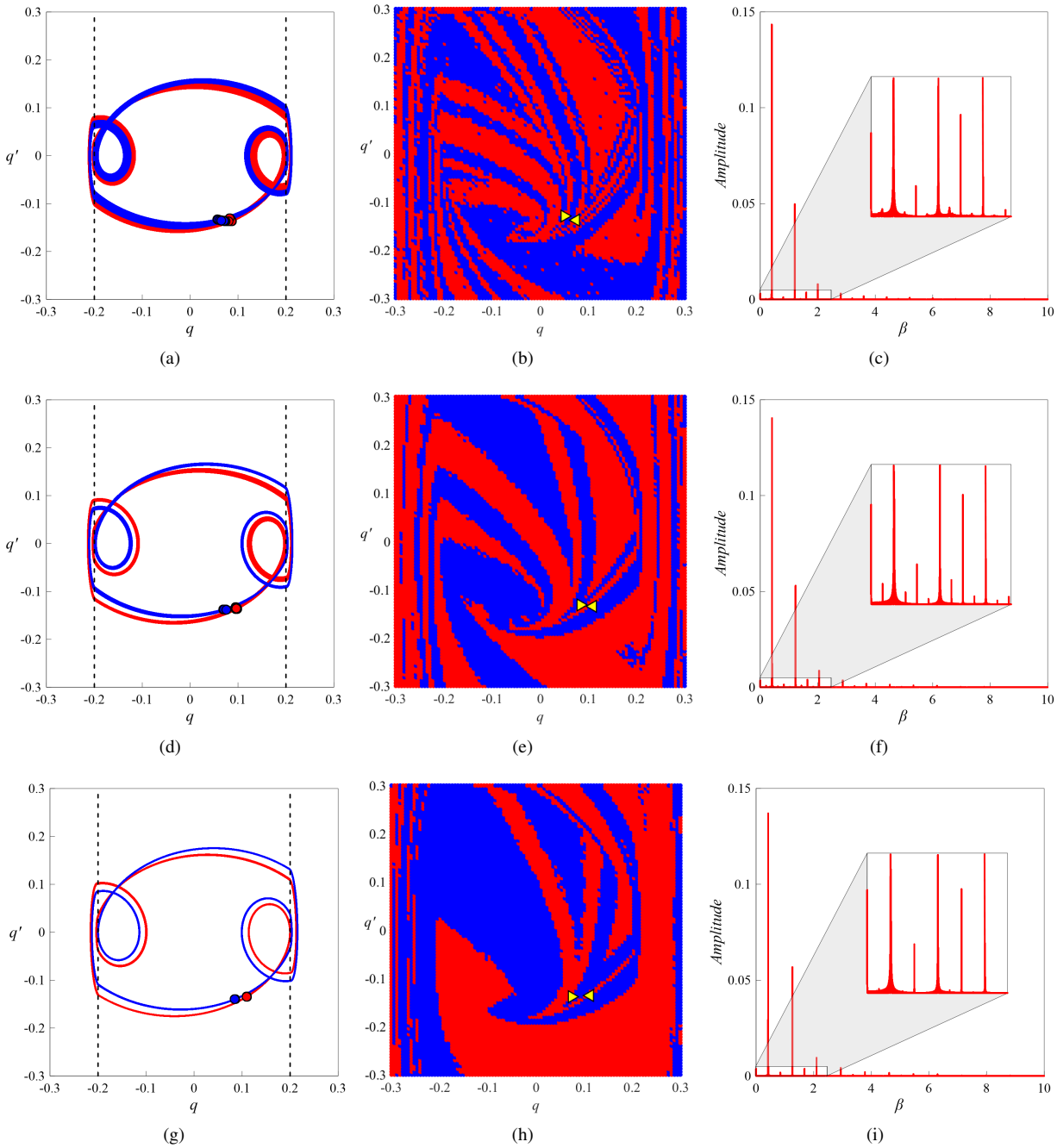

Figure 19: Region V ($\xi = 0.1$, $\gamma = 5$, $\lambda = 50$, $\delta_0 = \delta_0^*$) phase portraits with Poincaré sections: a) $\beta = 0.40$; d) $\beta = 0.41$; g) $\beta = 0.42$; basins of attraction: b) $\beta = 0.40$; e) $\beta = 0.41$; h) $\beta = 0.42$; Fourier spectra: c) $\beta = 0.40$; f) $\beta = 0.41$; i) $\beta = 0.42$.

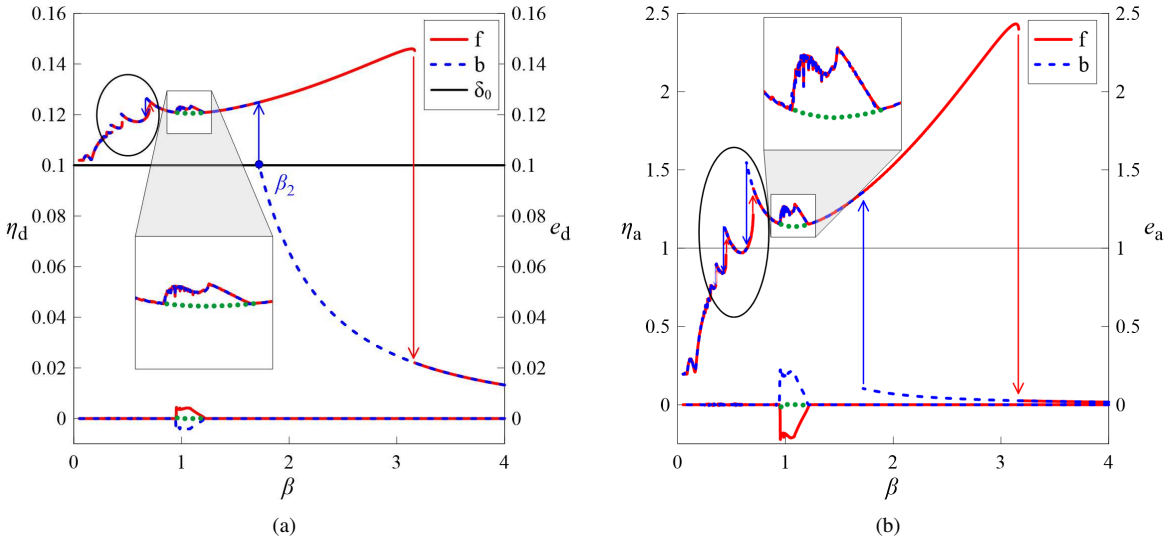

Figure 20: Region VI ($\xi = 0.1$, $\gamma = 5$, $\lambda = 50$, $\delta_0 = 0.1$), forward (solid red line) and backward (dashed blue line) PRCs of: a) η_d and e_d (curves in the lower part of the graph); b) η_a and e_a (curves in the lower part of the graph). The vertical arrows represent the jumps. The cascade of secondary resonances with left hysteresis is enclosed by the solid black ellipse, whereas a detail of the secondary non-regular resonance is shown in the zoomed square area.

In Fig. 20 the PRCs for $\delta_0 = 0.1$ are represented. It can observed that they are characterized by the occurrence of both the *primary resonance with right hysteresis* and different types of secondary resonances in the low frequency range. In particular, for $\beta < 0.9$, a *cascade of secondary resonances with left hysteresis* is observed (in Fig. 20 enclosed by an ellipse). Furthermore, in the neighbourhood of $\beta = 1$, a *secondary non-regular resonance* is noticed (rectangular zoomed area) and the eccentricity shows non-zero values. Unlike what was seen in Sect. 3.4 and 3.6, were the irregularity interval (Fig. 9 and 18) followed a *secondary resonance with right hysteresis*, here the *secondary non-regular resonance* is preceded by a *cascade of secondary resonances with left hysteresis*. In the low frequency range, where the *cascade of secondary resonance with left hysteresis* occurs (see the ellipse in Fig. 20), the eccentricity is always zero and the observed solutions, reached with a small number of forcing cycles, have the same period of the excitation ($n = 1$) and are characterized by the occurrence of several internal loops, which is reflected in a high number of impacts, increasing as β decreases. This can be seen better in Fig. 21(h), where the trend of the number of impacts per forcing cycle, against each bumper, is shown as β changes, both on the forward (increasing *beta*, solid red line) and on the backward (decreasing β, blue line) sweep. Some investigated β values are marked with colored dots and the corresponding phase portraits are represented above and below Fig. 21(h). In particular, the phase portraits corresponding to the valleys between the secondary resonances are depicted above, in Fig. 21(a), (c), (e) and (g), while the solutions observed in the secondary left hysteresis, just before the downward jumps in the backward sweep, denoted as ridges are shown below, in Fig. 21(b), (d) and (f). From Fig. 21(h), it can be noted that, starting from a valley (Fig. 21(a), for $\beta = 0.935$), in which the limit cycle has no internal loops and the mass hits each bumper once per forcing cycle, and following the backward sweep, that is decreasing β (dashed blue line in Fig. 21(h), from right to left), a pair of internal loops appears. They grow as β decreases and when they reach the obstacles (blue curve in Fig. 21(b), for $\beta = 0.64$), a sudden downward jump is observed. This results in an increase of 1 in the number of impacts per forcing cycle against each bumper (Fig. 21(c), for $\beta = 0.588$). By further decreasing β, another pair of internal loops appears. When even these loops reach the obstacles (blue curve in Fig. 21(d), for $\beta = 0.43$), another downward jump occurs, after which the numbers of impacts against each bumpers increases again by 1, and so on for the successive ridges and valleys (Fig. 21(e)-(g), for $\beta = 0.41$, $\beta = 0.345$ and $\beta = 0.326$ respectively). The limit cycle shown in Fig. 21(g) has six internal loops that intersect the obstacles and the number of impacts against each bumper per forcing cycle is equal to four. Conversely, starting from the valley shown in Fig. 21(g) and following the forward sweep, that is increasing β (solid red line in Fig. 21(h), from left to right), immediately after the upward jump, the two innermost loops move away from the obstacles (Fig. 21(f)); this results in a 1 drop in the number of impacts against

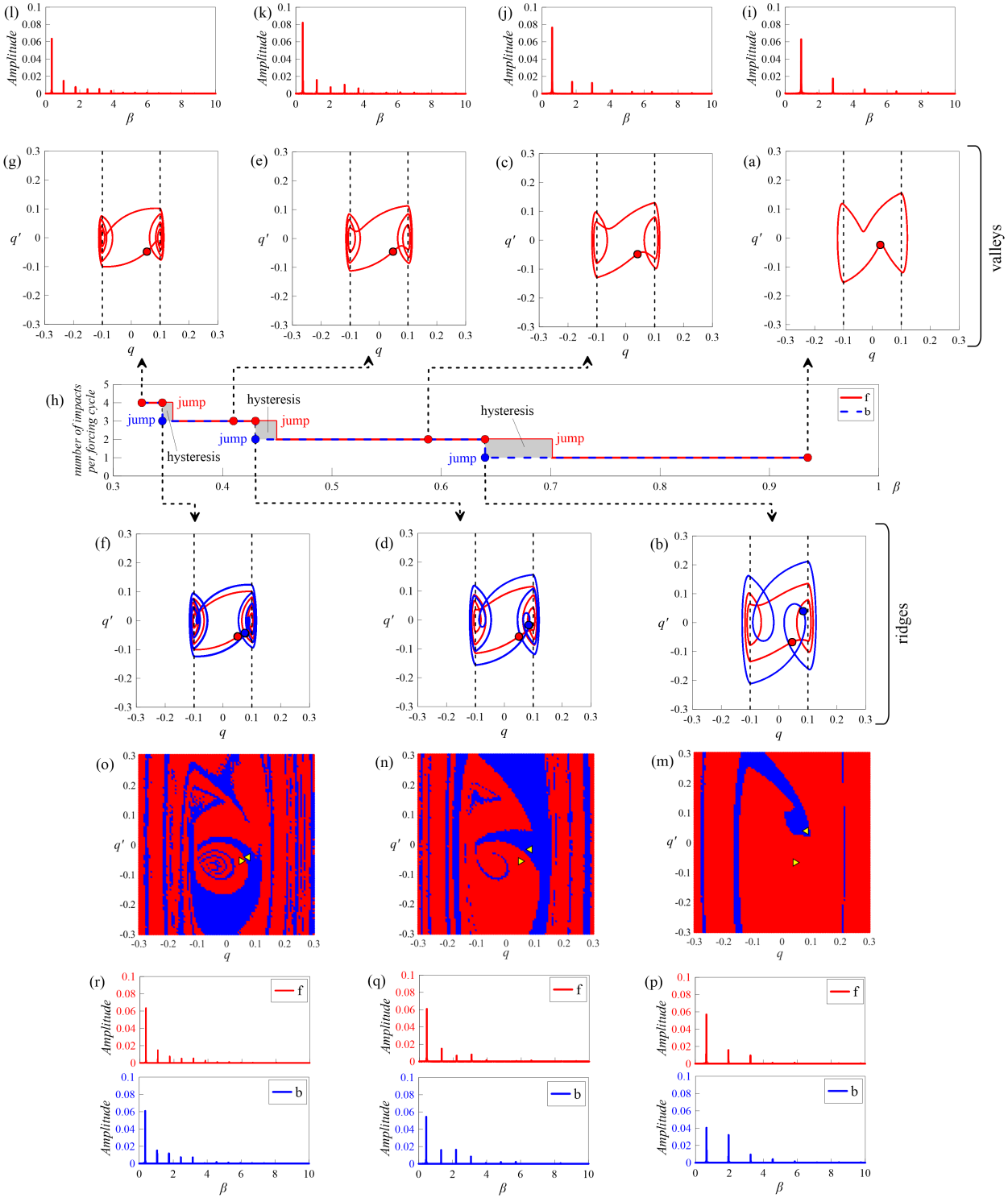

Figure 21: Region VI ($\xi = 0.1$, $\gamma = 5$, $\lambda = 50$, $\delta_0 = 0.1$): h) number of impacts against each bumper per forcing cycle *vs* β and example phase portraits with Poincaré sections, at steady-state, at the valleys (a, c, e, g) and at the ridges (secondary left hysteresis, just before the downward jump) (b, d, f). Basins of attraction at the ridges (m-o). Fourier spectra at the valleys (i-l) and at the ridges (p-r).

each bumper per forcing cycle. By further increasing β, this pair of loops progressively disappears. They transform themselves into cusps that gradually blunt, until another jump occurs. This again involves the moving away of the two innermost loops, of those left, from the obstacles (Fig. 21(e)) and the reduction of the number of impacts and so on, until all the inner loops disappear (Fig. 21(d)-(a)) and the mass returns to hit each bumper once (Fig. 21(a)). The Fourier spectra of the solutions observed at the valleys are shown in Fig. 21(i)-(l); they are characterized by the presence of several harmonic components, in addition to the fundamental one, whose number grows as β decreases. At the *secondary left hysteresis*, colored grey in Fig. 21(h), there are two steady-state solutions with impact (see Fig. 21(b), (d) and (f)): a large-amplitude motion (blue line) and a small-amplitude motion (red line). As for the primary right hysteresis, the third unstable solution was not obtained. Compared to the *primary resonance with right hysteresis*, here the large-amplitude motion is associated with the backward sweep (blue curve). Both the solutions are periodic, with the same period of the excitation ($n = 1$) and in the corresponding Fourier spectra (Fig. 21(p)-(r)), several harmonic components, in addition to the fundamental one, are observed. The basins of attraction are

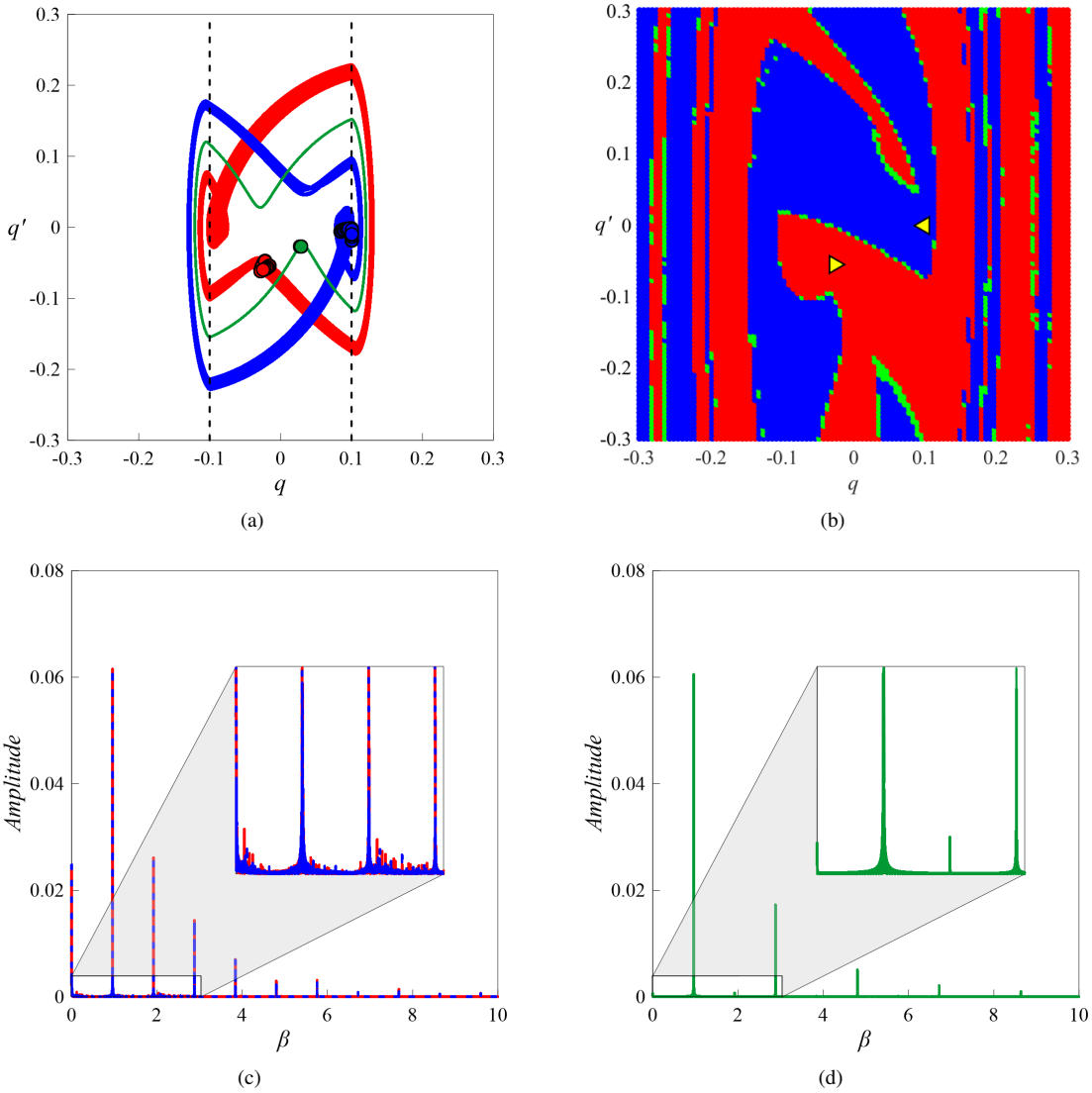

Figure 22: Region VI ($\xi = 0.1$, $\gamma = 5$, $\lambda = 50$, $\delta_0 = 0.1$, $\beta = 0.96$), secondary non-regular resonance: a) phase portraits with Poincaré sections; b) basins of attraction; Fourier spectra: c) pair of quasi-periodic solutions, solid red line for ($q_0 = -0.027$, $q_0' = -0.056$) and dashed blue line for ($q_0 = 0.1$, $q_0' = -0.002$); d) green solution for ($q_0 = 0.042$, $q_0' = -0.21$).

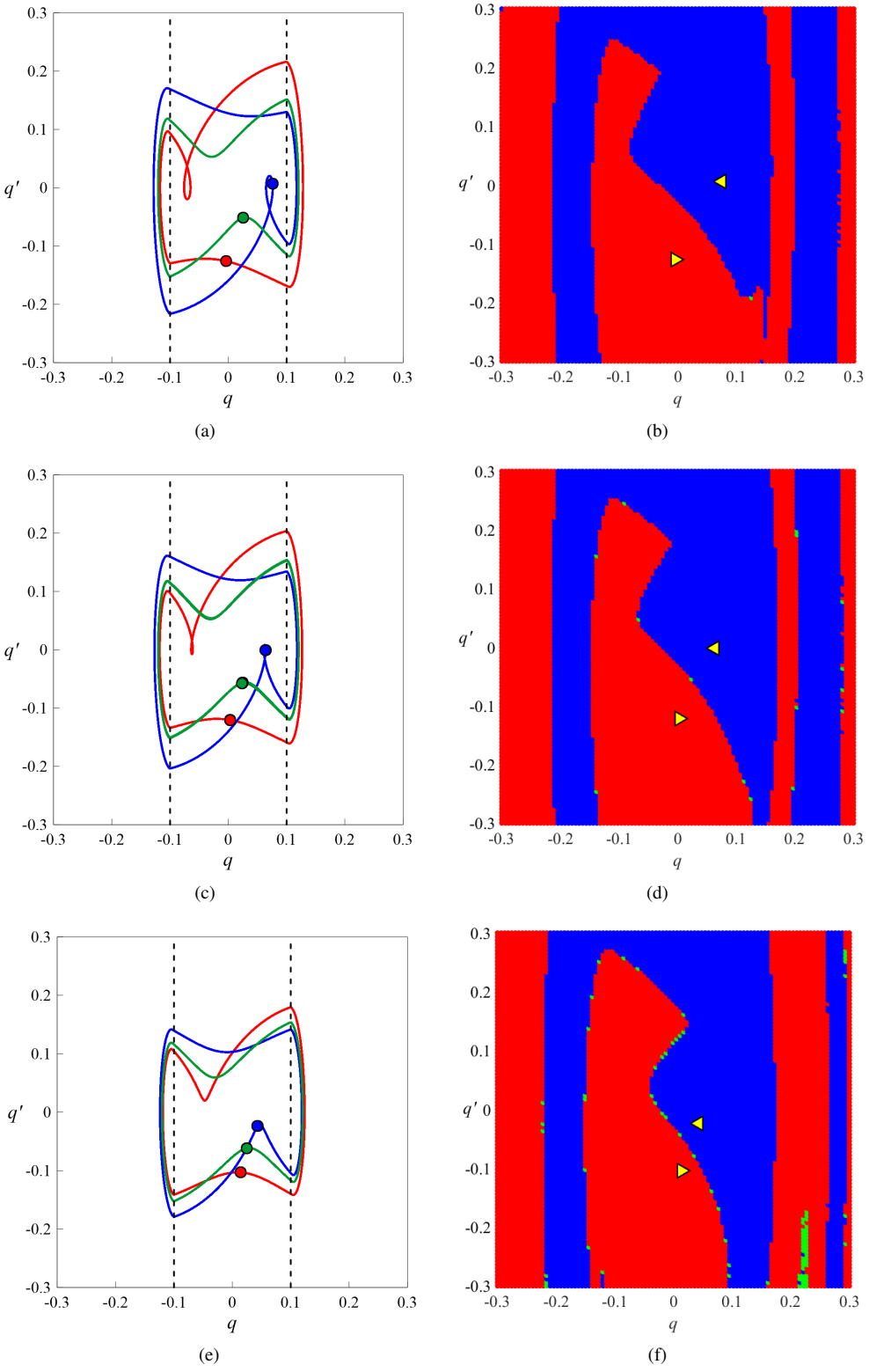

Figure 23: Region VI ($\xi = 0.1$, $\gamma = 5$, $\lambda = 50$, $\delta_0 = 0.1$) descending branch of the PRCs, after the secondary non-regular resonance, phase portraits with Poincaré sections: a) $\beta = 1.12$; c) $\beta = 1.14$; e) $\beta = 1.18$; basins of attraction: b) $\beta = 1.12$; d) $\beta = 1.14$; f) $\beta = 1.18$.

shown in Fig. 21(m)-(o) and are characterized by gradually more irregular (fractal) boundaries as β decreases. It can be observed that both the solutions have the same number of internal loops; however, while in the small-amplitude solution (red) all the loops intersect the obstacles, in the large-amplitude solution (blue) the innermost loops do not reach them. Consequently, the number of impacts on the forward sweep always exceeds the number of impacts on the backward sweep by 1 (see Fig. 21(h)). Decreasing β, the number of internal loops, an thus, the number of impacts per forcing cycle increases, both in the forward and in the backward sweep, with a greater number of impacts always on the forward sweep. Furthermore, the amplitude of the limit cycles decreases, the number of harmonic components increases and the basins of attraction become less regular, with a gradually decreasing extension of the basin of the smaller cycle (red basin). In the frequency range in correspondence with the *secondary non-regular resonance*, characterized by almost constant excursion, the same in both the forward and backward curve, and non-zero eccentricity, the existence of a *pair of quasi-periodic solutions*, with antisymmetric envelope, was observed (red and blue curves in Fig. 22(a), for $\beta = 0.96$). Each cycle that makes up the pair has an thick internal loop which, as time goes by, approaches, grazes, crosses and then moves away from one of the left vertical dashed line representing the position of the obstacle. In particular, the internal loop of the red cycle crosses only the left vertical dashed line (left bumper), while the internal loop of the blue cycle crosses only the right vertical dashed line (right bumper). This results, for each of the two solutions that make up the pair, in a different number of impacts, in each forcing cycle, to the right and left as time goes on. Given the quasi-periodic nature of the response, a high number of forcing cycles was required to reach a fairly stationary condition. By appropriately calibrating the initial conditions, and the number of forcing cycles, it is also possible to observe a periodic multi-frequency solution with $n = 1$, antisymmetric in itself (green curve in Fig. 22(a)), characterized by smaller excursion and zero eccentricity. In the PRCs (Fig. 20) the values of excursion and eccentricity, corresponding to this periodic limit cycle, are represented with green dots. They are placed on the ideal course of the PRC that would have occurred in the absence of the *secondary non-regular resonance*. The basins of attraction of the solutions are shown in Fig. 22(b). It can be observed that the initial conditions, corresponding to the periodic solution are located at the boundary between the basins of attraction of the cycles that make up the pair. The Fourier spectra of the two solutions that make up the pair (solid red and dashed blue lines in Fig. 22(c)) coincide and are characterized by several harmonic components. Since the limit cycles are weakly quasi-periodic, the incommensurate frequencies are much less obvious. These can be seen better in the rectangular zoomed areas. As concerns the periodic solution, the same commensurate harmonic components are observed (Fig. 22(d)), but some of them have much smaller amplitudes, compared to the two quasi-periodic solutions. Increasing β, the internal loops of the quasi-periodic solutions gradually move away from the obstacles, reducing the extent of the grazing. Consequently, the quasi-periodicity of the solutions, and thus the irregularity of the basins of attraction, decrease. Also the number of forcing cycles required to reach the stationary reduces. After passing the range characterized by almost constant excursion, a straight descending branch, along which there is a *pair of periodic solutions* with $n = 1$ (Fig. 23), is observed. Also in this frequency range, it is possible to observe a third periodic solution with $n = 1$ (green curve, similar to that shown in Fig. 21(a) and 22(a)), antisymmetric in itself, reachable starting from initial conditions that are placed on the boundaries of the basins of attraction of the other two solutions. The limit cycles that make up the pair initially have internal loops which no longer reach the obstacles (Fig. 23(a)); consequently, in each forcing cycle, the mass hits each bumper once. As β increases, these loops gradually disappear, taking on the appearance of cusps (Fig. 23(c)), progressively more rounded (Fig. 23(e)) and the solutions that make up the pair progressively become more and more similar to each other and to the third (green) solution. The basins of attraction (Fig. 23(b), (d) and (f)) return to have more regular boundaries, compared to Fig. 21(i)-(k) and 22(b), and no significant variations are observed with increasing β.

3.7.1. Further scenario

As anticipated in Sect. 3, for $0 < \delta_0 < \delta_0^*$, the observed scenarios are more varied and complex than those seen for $\delta_0^* < \delta_0 \leq 1$. An example of the possible situations that can be encountered inside Region VI has been shown in Sect. 3.7, for $\delta_0 = 0.1$. However, by slightly varying δ_0, quite different scenarios can be observed, like the one shown in Fig. 24, corresponding to $\delta_0 = 0.05$, which will be described below, without going into too much detail. It can be observed that, as for $\delta_0 = 0.1$ (Fig. 20), in the low frequency range, a *cascade* of similar secondary units was observed (enclosed by an ellipse). By analyzing the single unit, for example the largest one, in the range $0.96 \leq \beta \leq 1.71$ (rectangular zoomed area in Fig. 24), different homogeneous frequency ranges can be distinguished as β increases:

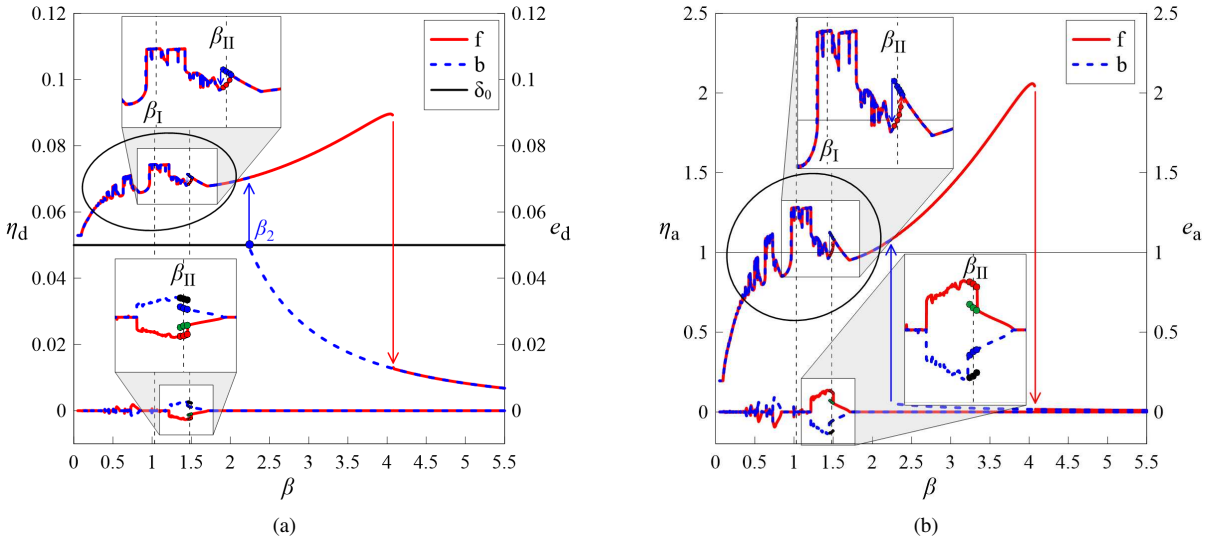

Figure 24: Region VI, further scenario ($\xi = 0.1$, $\gamma = 5$, $\lambda = 50$, $\delta_0 = 0.05$), forward (solid red line) and backward (dashed blue line) PRCs of: a) η_d and e_d (curves in the lower part of the graph); b) η_a and e_a (curves in the lower part of the graph). The vertical arrows represent the jumps. The cascade in the low frequency range is enclosed by the solid black ellipse, and a detail of one of the units in the cascade is shown in the two zoomed rectangular areas. The two dashed vertical lines represent β values that will be investigated in more detail.

- Range 1 ($0.963 \leq \beta \leq 1.214$) with a *secondary non-regular resonance*, approximatively zero-eccentricity and almost constant excursion;
- Range 2 ($1.214 < \beta < 1.45$) with a *secondary non-regular resonance*, non-zero-eccentricity and slightly decreasing excursion;
- Range 3 ($1.45 \leq \beta \leq 1.502$) with a *secondary resonance with left hysteresis* and non-zero eccentricity;
- Range 4 ($1.502 < \beta \leq 1.7$) with non-zero-eccentricity and decreasing excursion.

Within Range 1, a single chaotic solution, with antisymmetric envelope is observed (Fig. 25(a), for $\beta = \beta_I = 1.03$). The corresponding Fourier spectrum is shown in Fig. 25(b). It can be observed that the trajectory, during its chaotic evolution as time goes by, sometimes grazes the obstacles. Within Range 2, a *pair of quasi-periodic solutions*, similar to those shown in Fig. 22(a), is observed. Within Range 3, characterized by a left hysteresis with non-zero eccentricity, varying the initial conditions, *two pairs of periodic solutions*, (Fig. 26(a), for $\beta = \beta_{II} = 1.48$), each with $n = 1$, are observed. Each pair is associated with specific values of excursion and eccentricity and the corresponding basins of attraction are shown in Fig. 26(b). All four solutions have an internal loop. However, while in the pair associated with the forward sweep, the internal loop intersects the obstacle, in the pair associated with the backward sweep the loop does not reach it. Consequently, in each forcing cycle, the number of impacts on the forward sweep always exceeds the number of impact on the backward sweep by 1, as also observed in Sect. 3.7. In the PRCs (Fig. 24) the values of excursion and eccentricity, corresponding to the two pairs of periodic limit cycle, are represented with circular markers, and they can be seen better in the two zoomed rectangular areas. By focusing the attention on the eccentricity, it can be observed that, they are placed on four lines, two by two symmetrical with respect to the horizontal axis, respectively $e_d = 0$ and $e_a = 0$. Within Range 4, a *pair of periodic multi-frequency solutions*, with $n = 1$, is observed (similar to that shown in Fig. 23). The two solutions evolve with β in a similar way to what was described in the last part of Sect. 3.7. All the units in the *cascade* are similar to each other and are interspersed with frequency intervals characterized by a single periodic multi-frequency solution with $n = 1$. As observed in Sect. 3.7, decreasing β and moving from one valley to the other, the number of internal loops, and therefore of impacts, increases. By appropriately reducing the frequency increment $\Delta\beta$ of the sine sweep excitation, it is possible to observe, even in the smallest units, the left hysteresis, otherwise not visible. Also in this case, the difference between the left hysteresis belonging to different units lies in the number of internal loops in the limit cycles, and therefore in the

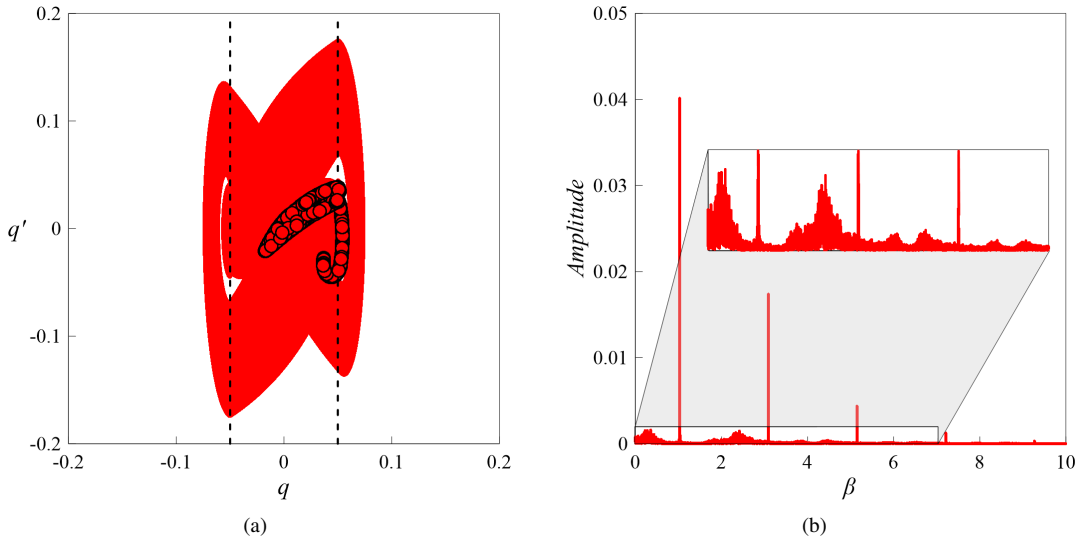

Figure 25: Region VI, further scenario ($\xi = 0.1$, $\gamma = 5$, $\lambda = 50$, $\delta_0 = 0.05$), Range 1, chaotic solution for $\beta = \beta_{\mathrm{I}} = 1.03$: a) phase portrait with Poincaré section; b) Fourier spectrum.

number of impacts. In particular, decreasing β, the number of internal loops and of impacts increases, with a number of impacts on the forward sweep which always exceeds the number of impact on the backward sweep by 1. In addition to the scenarios shown in Fig. 20 and 24, there may be many others. Given the complexity found within Region VI, it therefore deserves to be further investigated and this will be the aim of our future works.

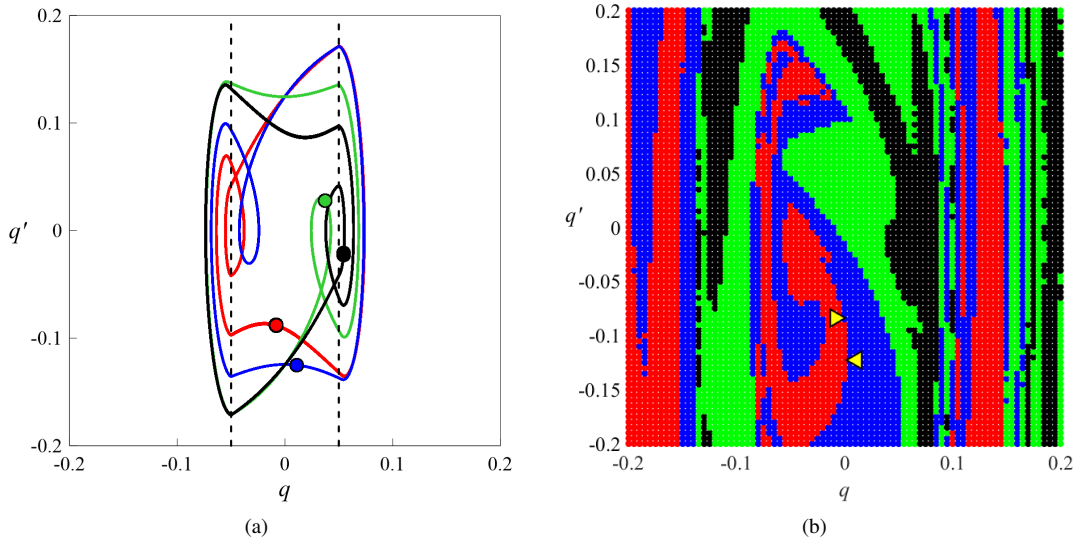

Figure 26: Region VI, further scenario ($\xi = 0.1$, $\gamma = 5$, $\lambda = 50$, $\delta_0 = 0.05$), Range 3, two pairs of periodic solutions $\beta = \beta_{\mathrm{II}} = 1.48$: a) phase portraits with Poincaré sections; b) basins of attraction. The first pair is made up of red and black solutions, the second pair is made up of blue and green solutions.

3.8. Region VII

In the limit case $\delta_0 = 0$, that is when the bumpers are initially in contact with the mass, the situation returns to be smooth (Fig. 27). Forward and backward PRCs overlap, without jumps, hysteresis or secondary resonances and the

primary resonance has moved to higher frequencies. Furthermore, eccentricity is always zero. However, the dynamic is different from that observed for $\delta_0 = 1$. Based on what was said in Sect. 2.4, impact occurs for each β value.

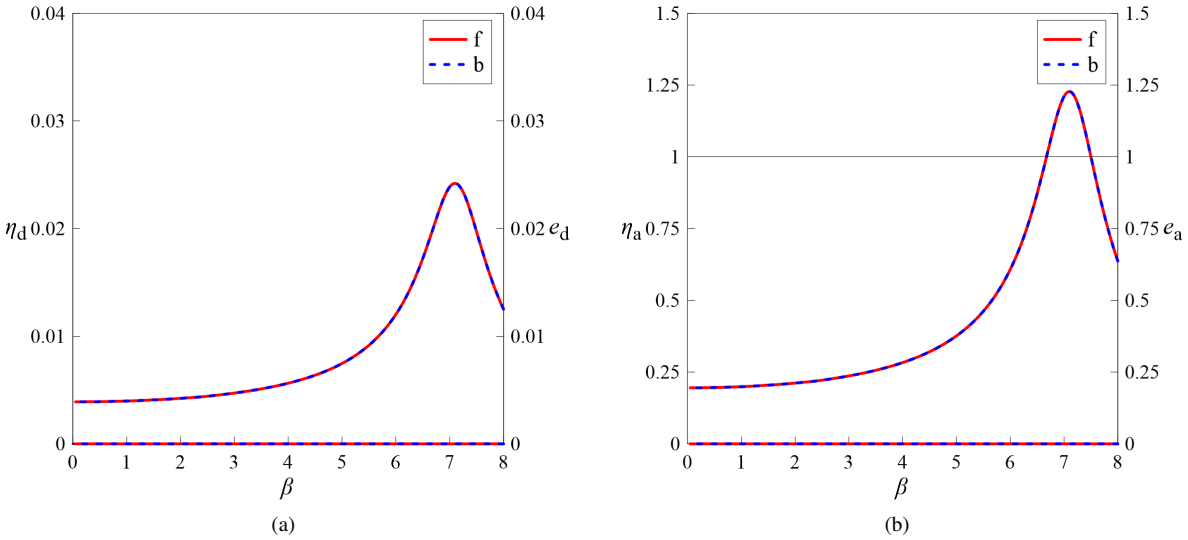

Figure 27: Region VII ($\xi = 0.1$, $\gamma = 5$, $\lambda = 50$, $\delta_0 = 0$), forward (solid red line) and backward (dashed blue line) PRCs of: a) η_d and e_d (curves in the lower part of the graph); b) η_a and e_a (curves in the lower part of the graph).

It can be observed that the values of excursion of relative displacement η_d are much smaller than those corresponding to the other previously considered values of δ_0. For each β value a periodic mono-frequency solution, with the same period of the excitation, that is $n = 1$, is observed (Fig. 28(a)). Consequently, at steady-state, reached with a small number of forcing cycles, the points in the Poincaré sections coincide with a single point. The limit cycle takes on the appearance of a very flattened ellipse and in the Fourier spectra (Fig. 28(b)), only the fundamental harmonic component is observed.

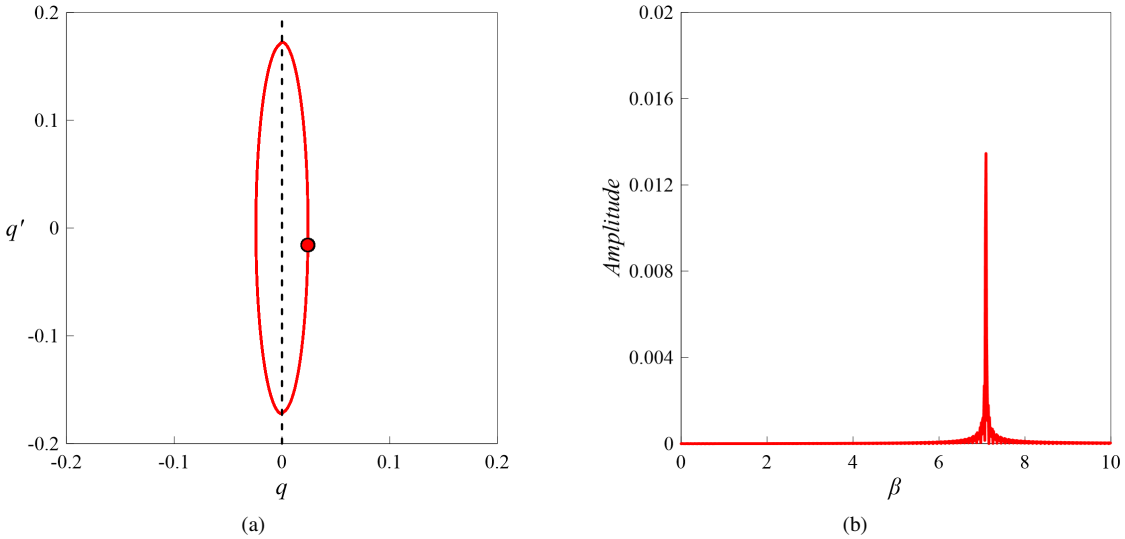

Figure 28: Region VII ($\xi = 0.1$, $\gamma = 5$, $\lambda = 50$, $\delta_0 = 0$): a) phase portrait with Poincaré section and b) Fourier spectrum for $\beta = 7.1$.

Given the fairly small value of the relaxation time of the considered bumpers compared to the forcing period ($\tau_r = 0.02$), it is difficult to see the flight phases between consecutive contacts. In fact, the duration of each flight

phase is very short, because the detachment between the mass and the single bumper takes place when the latter has recovered practically all its deformation and immediately afterwards the mass impacts the other bumper, which in the meantime has already recovered its deformation.

3.9. Summary

In Sect. 2.4, it was shown that, once the value of the damping ratio ξ has been set, it is possible to analytically determine, resorting to geometric considerations, the frequency interval in which impact surely will occur ($\beta_1 \leq \beta \leq \beta_2$), for a given value of δ_0 (see the yellow horizontal lines in Fig. 3(b)). Due to the mainly hardening behavior of the considered vibro-impact system, this frequency range, highlighted in yellow in Fig. 29(a), extends to the right (green region). The green region is bounded by the descending branch of the PRC, after the resonance, which represents the locus of β_2 values, and the thin dotted black curve which represents the locus of the downward jumps frequencies in the forward sweep (denoted as β_{jump}). While if $\beta_1 \leq \beta \leq \beta_2$ the impact will surely occur for geometric reasons, if $\beta_2 \leq \beta \leq \beta_{\text{jump}}$ it will occur, due to the nonlinear behavior of the system, and depending on the values of the parameters and the initial conditions. In the same figure, the horizontal dashed lines represent the investigated δ_0 values and the red and blue dots indicate the corresponding values of β_1 and β_2. Finally, the identified regions are shown on the left, with Roman numerals enclosed within circles.

In the previous Sections, for each considered δ_0 value, and for $\xi = 0.1$, $\gamma = 5$ and $\lambda = 50$, starting from the analysis of the PRCs, homogeneous frequency intervals, characterized by similar features in terms of number and type of observed solutions, presence or absence of hysteresis and eccentricity, were identified. In Fig. 29(b) these frequency ranges are represented with colored horizontal bars. Within the single horizontal bar, every color represents a homogeneous β interval and a brief description of its main characteristics is given in the legend shown at the bottom of Fig. 29. The limits of the sub-ranges must be understood as qualitative, especially in the low frequency range. Furthermore, it is worth noting that these colors have nothing to do with those used in Fig. 4 to distinguish the regions in the $\lambda - \delta_0$ plane. By stacking, one below the other, the frequency intervals corresponding to the investigated values of δ_0, and thanks to the use of different colors, it is possible to have an overview of the encountered scenarios and to get an idea of the possible evolution of the different secondary behaviors, as δ_0 decreases, starting from the free flight condition ($\delta_0 = 1$). It can be observed that in the two limit cases, that is $\delta_0 = 1$ (Region I) and $\delta_0 = 0$ (Region VII), the situation is smooth, although the dynamic is different. Indeed, in the first case ($\delta_0 = 1$) impact does not occur for any β value, whereas in the second case ($\delta_0 = 0$) impact occurs for each β value. Leaving out the frequency range characterized by the absence of impact, left white, it can be noted that decreasing δ_0, the amplitude of the frequency range associated with the occurrence of impacting solutions (colored bars) increases. Also the number of used colors, and therefore of encountered behaviors, increases, especially in the low frequency range and for $0 < \delta_0 < \delta_0^*$. Yellow and green colors appear to prevail over the others. The former represents the frequency range associated with the occurrence of a single periodic impacting solution with $n = 1$ or $n = 3$, while the latter corresponds to the *primary right hysteresis*. It can be observed that, starting from the absence of hysteresis for $\delta_0 = 1$ (forward and backward PRCs overlap), this frequency range increases and finally disappears again for $\delta_0 = 0$ (forward and backward PRCs overlap again). The other colors were used to represent the smaller frequency ranges corresponding to the observed secondary resonances. As can be seen from Fig. 29(b), and as already noted in Sect. 3, the reference value $\delta_0 = \delta_0^*$ seems to represents the watershed between different types of observed behaviors. Indeed, for $\delta_0^* \leq \delta_0 < 1$, the situation is quite calm, except for very small frequency ranges in which *secondary resonances with right hysteresis*, followed by intervals with non-zero eccentricity, were observed (for $\delta = 0.4$, inside Region IV and for $\delta = \delta_0^*$, inside Region V). Conversely, more complex and varied scenarios (with *secondary resonances with left hysteresis*, *secondary non-regular resonances* and *cascades* of similar behaviors), which reflect in a greater chromatic variety, were observed for $0 < \delta_0 < \delta_0^*$ (inside Region VI). These secondary behaviors affect gradually wider frequency ranges as the δ_0 decreases. Despite the great variety of identified homogeneous frequency intervals, the use of colors allows to recognize a certain regularity and to highlight the presence of *cascades* of behaviors that are repeated on different scales, keeping a similar shape. In particular, the *cascade of secondary left hysteresis*, for $\delta_0 = 0.1$, highlighted in blue, and the *cascade* of more complex secondary units (formed by the adjacent cyan, red, purple and grey ranges, corresponding to the four ranges defined in Sect. 3.7.1) observed for $\delta_0 = 0.05$. For values of $0 < \delta_0 \leq \delta_0^*$, internal loops in the phase portraits were also observed. These loops, in the low frequency range, often reach and cross the obstacles, giving rise to number of impacts per forcing cycle, against each bumper, greater than one. As β decreases, these loops gradually increase in number, and thus also the number of impact increases.

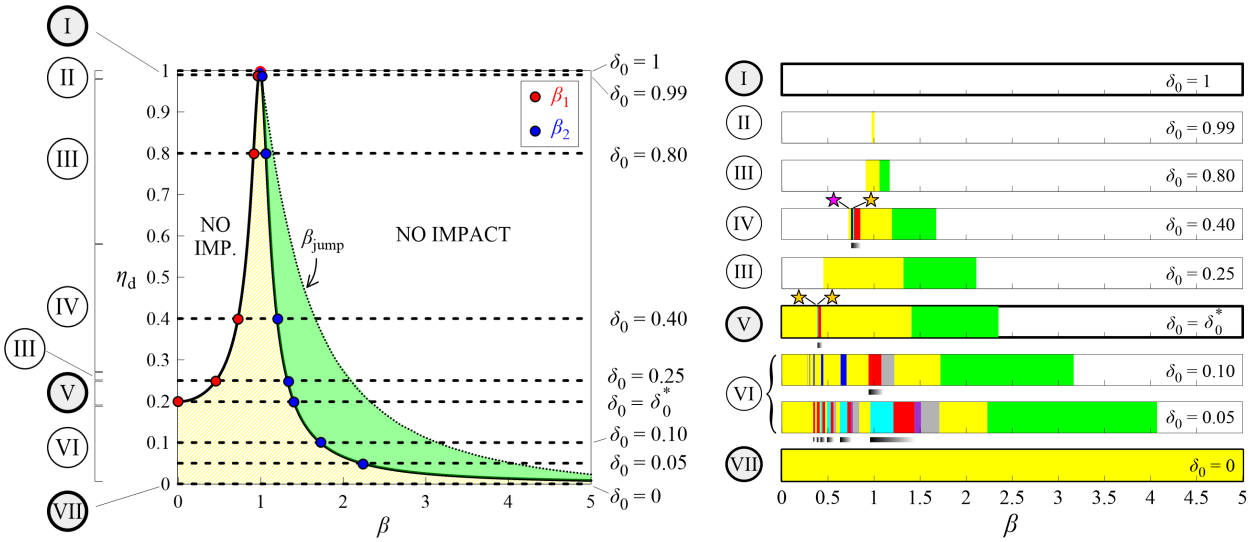

LEGEND

Color	Impact	Eccentricity	Hysteresis	Solutions
	no	$e = 0$	-	a single periodic non-impacting solution ($n = 1$)
	yes	$e = 0$	-	a single periodic impacting solution ($n = 1$ or 3)
	yes	$e = 0$	primary right hysteresis	two coexisting periodic solutions ($n = 1$): a large-amplitude impacting motion (forward sweep) and a small-amplitude non-impacting motion (backward sweep)
	yes	$e = 0$	secondary right hysteresis	two coexisting impacting solutions: a periodic solution ($n = 3$) and a quasi-periodic solution
	yes	$e = 0$	-	a single quasi-periodic or chaotic impacting solution
	yes	$e \neq 0$	-	a pair of quasi-periodic impacting solutions with antisymmetric envelope, with or without a coexisting periodic impacting solution ($n = 1$)
	yes	$e = 0$	secondary left hysteresis	two coexisting periodic impacting solutions ($n = 1$): a large-amplitude motion (backward sweep) and a small-amplitude motion (forward sweep)
	yes	$e \neq 0$	-	a pair of periodic ($n = 1$) impacting solutions with antisymmetric envelope, with or without a coexisting periodic impacting solution ($n = 1$)
	yes	$e \neq 0$	-	two pairs of periodic impacting solutions ($n = 1$), each with antisymmetric envelope

Figure 29: a) PRC of normalized excursion of relative displacement η_d in free flight condition for $\xi = 0.1$ (thick black curve) with indication of the frequency intervals in which impact surely will occur (yellow) or in which it will occur depending on the initial conditions (green); the dashed horizontal lines represent the investigated δ_0 values and the Roman numerals enclosed within circles indicate the regions. b) Homogeneous frequency intervals corresponding to the investigated δ_0 values (for $\xi = 0.1$, $\gamma = 5$, $\lambda = 50$). The magenta star denotes the occurrence of primary grazing, whereas the orange stars correspond to the secondary grazing and the shaded black bands highlight the frequency intervals characterized by the occurrence of grazing. A summary of the main features of each frequency interval is given in the legend below.

Therefore, while for $\delta_0^* \leq \delta_0 < 1$ neither *cascades*, nor *secondary resonances with left hysteresis* were observed, but only *secondary resonances with right hysteresis* localized in a small frequency interval, for $0 < \delta_0 < \delta_0^*$ no *secondary right hysteresis* were observed and the secondary resonances affect wider frequency ranges. Furthermore, this study allowed to observe that, in the considered model, the *grazing phenomenon* plays an important role, and it is related to the occurrence of some of the observed scenarios. In particular, in Fig. 29(b) the occurrence of *primary* and *secondary grazing* is highlighted with magenta and orange stars respectively, whereas the shaded black bands represent the frequency intervals in which the trajectories graze the obstacles as time goes by and the extent of grazing decreases as β increases.

4. Conclusions and future developments

In this paper, some of the scenarios that can occur in the numerical nonlinear non-smooth response of a SDOF system, symmetrically constrained by deformable and dissipative bumpers, under a harmonic base excitation, with the variation of selected parameters, were identified and investigated. In the numerical model, both the damper and the bumpers were modeled with the Kelvin-Voigt model. The model is described in terms of dimensionless parameters and, due to the adopted normalization, the damping ratio plays a fundamental role by influencing both the response of the system and the amplitude of the base excitation. By observing the characteristics of the PRCs of excursion and eccentricity of absolute acceleration and relative displacement of the mass, obtained for fixed values of ξ and γ and considering a sine sweep base excitation, seven homogeneous regions in the $\lambda - \delta_0$ plane, each corresponding to a scenario, were identified. Subsequently, referring to a constant value of the stiffness ratio λ, each scenario, corresponding to a different value of the dimensionless gap δ_0, was investigated resorting to phase portraits and Fourier spectra. In some cases, further analysis varying the initial conditions (basins of attraction) were carried out. Within each scenario, homogeneous frequency intervals, characterized by similar features in terms of number (single solution, *coexisting solutions* or *pair of solutions*) and types of limit cycles (*periodic*, *quasi-periodic* or *chaotic*), were identified. Decreasing the dimensionless gap, starting from $\delta_0 = 1$, gradually more complex and varied scenarios, characterized by the presence of the *primary resonance with right hysteresis* and also by the occurrence of different types of *secondary resonances* (with *right* or *left hysteresis* or of *non-regular* type) and *cascades*, affecting gradually wider frequency ranges, were observed. The occurrence of the (*primary* and *secondary*) grazing phenomenon, and its relation with some of the observed situations, was also highlighted. A reference value for the dimensionless gap, denoted as δ_0^*, was identified. It allowed to distinguish some δ_0 ranges (namely $\delta_0 = 1$, $\delta_0^* < \delta_0 < 1$, $0 < \delta_0 < \delta_0^*$ and $\delta_0 = 0$) in which different behaviors were observed. In particular, the most complex scenarios were noticed for $0 < \delta_0 < \delta_0^*$. Conversely, for $\delta_0^* \leq \delta_0 < 1$, more calm situations were observed. In the two limit cases ($\delta_0 = 1$ and $\delta_0 = 0$), the situation is instead smooth, although characterized by different dynamics. Based on the results obtained in this work and in [69], a future development of this study will be to investigate in more detail the part of the $\lambda - \delta_0$ plane where the identified regions converge (enclosed within a circle in Fig. 4), and to deepen the study of Region VI, which has proven to be particularly complex and rich in behaviors. Furthermore, based on the indications provided by the numerical model, a further experimental laboratory campaign will be carried out to confirm the numerical results, especially for small, null and negative values of the dimensionless gap.

Declaration of Competing Interest

None

References

[1] R. A. Ibrahim, Vibro-Impact Dynamics: Modeling, Mapping and Applications, Vol. 43, Springer, 2009.

[2] Y. Liu, M. Wiercigroch, E. Pavlovskaia, Z. Peng, Forward and backward motion control of a vibro-impact capsule system, Int. J. Non. Linear. Mech. 70 (2015) 30–46. doi:10.1016/j.ijnonlinmec.2014.10.009.

[3] Y. Liu, E. Pavlovskaia, M. Wiercigroch, Experimental verification of the vibro-impact capsule model, Nonlinear Dyn. 83 (1-2) (2016) 1029–1041. doi:10.1007/s11071-015-2385-6.

[4] Y. Yan, Y. Liu, M. Liao, A comparative study of the vibro-impact capsule systems with one-sided and two-sided constraints, Nonlinear Dyn. 89 (2) (2017) 1063–1087. doi:10.1007/s11071-017-3500-7.

[5] X. D. Gu, Z. C. Deng, Dynamical analysis of vibro-impact capsule system with Hertzian contact model and random perturbation excitations, Nonlinear Dyn. 92 (4) (2018) 1781–1789. doi:10.1007/s11071-018-4161-x.

[6] Y. Yan, Y. Liu, L. Manfredi, S. Prasad, Modelling of a vibro-impact self-propelled capsule in the small intestine, Nonlinear Dyn. 96 (1) (2019) 123–144. doi:10.1007/s11071-019-04779-z.

[7] S. Divenyi, M. A. Savi, M. Wiercigroch, E. Pavlovskaia, Drill-string vibration analysis using non-smooth dynamics approach, Nonlinear Dyn. 70 (2) (2012) 1017–1035. doi:10.1007/s11071-012-0510-3.

[8] X. Liu, N. Vlajic, X. Long, G. Meng, B. Balachandran, Nonlinear motions of a flexible rotor with a drill bit: Stick-slip and delay effects, Nonlinear Dyn. 72 (1-2) (2013) 61–77. doi:10.1007/s11071-012-0690-x.

[9] X. Liu, N. Vlajic, X. Long, G. Meng, B. Balachandran, Coupled axial-torsional dynamics in rotary drilling with state-dependent delay: stability and control, Nonlinear Dyn. 78 (3) (2014) 1891–1906. doi:10.1007/s11071-014-1567-y.

[10] Y. Liu, J. Páez Chávez, R. De Sa, S. Walker, Numerical and experimental studies of stickslip oscillations in drill-strings, Nonlinear Dyn. 90 (4) (2017) 2959–2978. doi:10.1007/s11071-017-3855-9.

[11] V. Vaziri, M. Kapitaniak, M. Wiercigroch, Suppression of drill-string stick-slip vibration by sliding mode control: Numerical and experimental studies, Eur. J. Appl. Math. 29 (5) (2018) 805–825. doi:10.1017/S0956792518000232.
[12] L. P. de Moraes, M. A. Savi, Drill-string vibration analysis considering an axial-torsional-lateral nonsmooth model, J. Sound Vib. 438 (2019) 220–237. doi:10.1016/j.jsv.2018.08.054.
[13] P. K. Malhotra, Dynamics of seismic impacts in base-isolated buildings, Earthq. Eng. Struct. Dyn. 26 (8) (1997) 797–813. doi:10.1002/(SICI)1096-9845(199708)26:8<797::AID-EQE677>3.0.CO;2-6.
[14] P. Komodromos, P. C. Polycarpou, L. Papaloizou, M. C. Phocas, Response of seismically isolated buildings considering poundings, Earthq. Eng. Struct. Dyn. 36 (12) (2007) 1605–1622. doi:10.1002/eqe.692.
[15] P. C. Polycarpou, P. Komodromos, On poundings of a seismically isolated building with adjacent structures during strong earthquakes, Earthq. Eng. Struct. Dyn. 39 (2010) 933–940. doi:10.1002/eqe.975.
[16] P. C. Polycarpou, P. Komodromos, Earthquake-induced poundings of a seismically isolated building with adjacent structures, Eng. Struct. 32 (7) (2010) 1937–1951. doi:10.1016/j.engstruct.2010.03.011.
[17] A. Masroor, G. Mosqueda, Experimental simulation of base-isolated buildings pounding against moat wall and effects on superstructure response, Earthq. Eng. Struct. Dyn. 41 (14) (2012) 2093–2109. doi:10.1002/eqe.2177.
[18] A. Masroor, G. Mosqueda, Impact model for simulation of base isolated buildings impacting flexible moat walls, Earthq. Eng. Struct. Dyn. 42 (2013) 357–376. doi:10.1002/eqe.2210.
[19] E. A. Mavronicola, P. C. Polycarpou, P. Komodromos, Effect of planar impact modeling on the pounding response of base-isolated buildings, Front. Built Environ. 2 (11) (2016) 1–16. doi:10.3389/fbuil.2016.00011.
[20] R. Jankowski, K. Wilde, Y. Fujino, Reduction of pounding effects in elevated bridges during earthquakes, Earthq. Eng. Struct. Dyn. 29 (2) (2000) 195–212. doi:10.1002/(SICI)1096-9845(200002)29:2<195::AID-EQE897>3.0.CO;2-3.
[21] A. X. Guo, Z. J. Li, H. Li, J. P. Ou, Experimental and analytical study on pounding reduction of base isolated highway bridges using MR dampers, Earthq. Eng. Struct. Dyn. 38 (11) (2009) 1307–1333. doi:10.1002/eqe.903.
[22] H. Hao, K. Bi, N. Chouw, W. X. Ren, State-of-the-art review on seismic induced pounding response of bridge structures, J. Earthq. Tsunami 7 (3) (2013) 1–19. doi:10.1142/S179343111350019X.
[23] C. Alhan, H. P. Gavin, Reliability of base isolation for the protection of critical equipment from earthquake hazards, Eng. Struct. 27 (9) (2005) 1435–1449. doi:10.1016/j.engstruct.2005.04.007.
[24] M. Hamidi, M. El Naggar, On the performance of SCF in seismic isolation of the interior equipment of buildings, Earthq. Eng. Struct. Dyn. 36 (2007) 1581–1604. doi:10.1002/eqe.708.
[25] L. Y. Lu, G. L. Lin, Predictive control of smart isolation system for precision equipment subjected to near-fault earthquakes, Eng. Struct. 30 (11) (2008) 3045–3064. doi:10.1016/j.engstruct.2008.04.016.
[26] M. Ismail, J. Rodellar, F. Ikhouane, An innovative isolation bearing for motion-sensitive equipment, J. Sound Vib. 326 (3-5) (2009) 503–521. doi:10.1016/j.jsv.2009.06.022.
[27] A. Reggio, M. De Angelis, Optimal design of an equipment isolation system with nonlinear hysteretic behavior, Earthq. Eng. Struct. Dyn. 42 (2013) 1907–1930. doi:10.1002/eqe.2304.
[28] A. Reggio, M. De Angelis, Combined primary-secondary system approach to the design of an equipment isolation system with High-Damping Rubber Bearings, J. Sound Vib. 333 (9) (2014) 2386–2403. doi:10.1016/j.jsv.2013.12.006.
[29] A. Sarebanha, G. Mosqueda, M. K. Kim, J. H. Kim, Seismic response of base isolated nuclear power plants considering impact to moat walls, Nucl. Eng. Des. 328 (January) (2018) 58–72. doi:10.1016/j.nucengdes.2017.12.021.
[30] P. C. Polycarpou, P. Komodromos, Numerical investigation of potential mitigation measures for poundings of seismically isolated buildings, Earthq. Struct. 2 (1) (2011) 1–24. doi:10.12989/eas.2011.2.1.001.
[31] P. C. Polycarpou, P. Komodromos, A. C. Polycarpou, A nonlinear impact model for simulating the use of rubber shock absorbers for mitigating the effects of structural pounding during earthquakes, Earthq. Eng. Struct. Dyn. 42 (1) (2013) 81–100. doi:10.1002/eqe.2194.
[32] E. Renzi, M. De Angelis, Optimal semi-active control and non-linear dynamic response of variable stiffness structures, J. Vib. Control 11 (10) (2005) 1253–1289. doi:10.1177/1077546305054597.
[33] H. P. Gavin, A. Zaicenco, Performance and reliability of semi-active equipment isolation, J. Sound Vib. 306 (1-2) (2007) 74–90. doi:10.1016/j.jsv.2007.05.039.
[34] A. Arena, W. Lacarbonara, A. Casalotti, Payload oscillations control in harbor cranes via semi-active vibration absorbers: Modeling, simulations and experimental results, Procedia Eng. 199 (2017) 501–509. doi:10.1016/j.proeng.2017.09.136.
[35] K. L. Johnson, Contact Mechanics, Cambridge University Press, Cambridge, UK, 1985.
[36] W. Goldsmith, Impact: The Theory and Physical Behavior of Colliding Solids, Edward Arnold Ltd., London, England, 1960.
[37] S. Muthukumar, R. DesRoches, A Hertz contact model with non-linear damping for pounding simulation, Earthq. Eng. Struct. Dyn. 35 (2006) 811–828. doi:10.1002/eqe.557.
[38] M. Machado, P. Moreira, P. Flores, H. M. Lankarani, Compliant contact force models in multibody dynamics: Evolution of the Hertz contact theory, Mech. Mach. Theory 53 (2012) 99–121. doi:10.1016/j.mechmachtheory.2012.02.010.
[39] L. Skrinjar, J. Slavi, A review of continuous contact-force models in multibody dynamics, Int. J. Mech. Sci. 145 (2018) 171–187. doi:10.1016/j.ijmecsci.2018.07.010.
[40] P. Flores, M. Machado, M. T. Silva, J. M. Martins, On the continuous contact force models for soft materials in multibody dynamics, Multibody Syst. Dyn. 25 (2011) 357–375. doi:10.1007/s11044-010-9237-4.
[41] P. Flores, H. M. Lankarani, Contact Force Models for Multibody Dynamics, Springer, 2016.
[42] H. Hertz, Über die Berührung fester elastischer Körper, J. für die reine und Angew. Math. 91 (1881) 156–171.
[43] L. Pust, F. Peterka, Impact oscillator with Hertz's model of contact, Meccanica 38 (2003) 99–114. doi:10.1023/A:1022075519038.
[44] F. Dubowsky, S. Freudenstein, Dynamic Analysis of Mechanical Systems With Clearances - Part 1: Formation of Dynamic Model, J. Eng. Ind. 93 (1) (1971) 305–309. doi:10.1115/1.3427895.
[45] Y. A. Khulief, A. A. Shabana, A continuous force model for the impact analysis of flexible multibody systems, Mech. Mach. Theory 22 (3) (1987) 213–224. doi:10.1016/0094-114X(87)90004-8.

[46] K. Hunt, E. Crossley, Coefficient of restitution interpreted as damping in vibroimpact, J. Appl. Mech. Am. Soc. Mech. Eng. 42 (2) (1975) 440–445. doi:10.1115/1.3423596.
[47] D. J. Wagg, S. R. Bishop, Chatter, sticking and chaotic impacting motion in a two-degree of freedom impact oscillator, Int. J. Bifurcat. Chaos 11 (1) (2001) 57–71. doi:10.1142/S0218127401001943.
[48] D. J. Wagg, S. R. Bishop, Dynamics of a two degree of freedom vibro-impact system with multiple motion limiting constraints 14 (1) (2004) 119–140. doi:10.1142/S0218127404009223.
[49] G. W. Luo, X. H. Lv, Y. Q. Shi, Vibro-impact dynamics of a two-degree-of freedom periodically-forced system with a clearance: Diversity and parameter matching of periodic-impact motions, Int. J. Non. Linear. Mech. 65 (2014) 173–195. doi:10.1016/j.ijnonlinmec.2014.04.013.
[50] G. W. Luo, X. F. Zhu, Y. Q. Shi, Dynamics of a two-degree-of freedom periodically-forced system with a rigid stop: Diversity and evolution of periodic-impact motions, J. Sound Vib. 334 (2015) 338–362. doi:10.1016/j.jsv.2014.08.029.
[51] Z. Hao, Q. Cao, M. Wiercigroch, Two-sided damping constraint control strategy for high-performance vibration isolation and end-stop impact protection, Nonlinear Dyn. 86 (4) (2016) 2129–2144. doi:10.1007/s11071-016-2685-5.
[52] T. Luo, Z. Wang, Periodically forced system with symmetric motion limiting constraints: Dynamic characteristics and equivalent electronic circuit realization, Int. J. Non. Linear. Mech. 81 (2016) 283–302. doi:10.1016/j.ijnonlinmec.2016.01.021.
[53] H. Jiang, A. S. Chong, Y. Ueda, M. Wiercigroch, Grazing-induced bifurcations in impact oscillators with elastic and rigid constraints, Int. J. Mech. Sci. 127 (May 2016) (2017) 204–214. doi:10.1016/j.ijmecsci.2017.02.001.
[54] J. Wang, Y. Shen, S. Yang, Dynamical analysis of a single degree-of-freedom impact oscillator with impulse excitation, Adv. Mech. Eng. 9 (7) (2017) 1–10. doi:10.1177/1687814017716619.
[55] H. Gritli, S. Belghith, Diversity in the nonlinear dynamic behavior of a one-degree-of-freedom impact mechanical oscillator under OGY-based state-feedback control law: Order, chaos and exhibition of the border-collision bifurcation, Mech. Mach. Theory 124 (2018) 1–41. doi:10.1016/j.mechmachtheory.2018.02.001.
[56] J. Chen, F. Min, Q. Jin, B. Ye, Coexistence, bifurcation and chaos of a periodically forced duffing system with absolute nonlinearity, Eur. Phys. J. Spec. Top. 228 (6) (2019) 1405–1419. doi:10.1140/epjst/e2019-800221-1.
[57] G. F. S. Rebouças, I. F. Santos, J. J. Thomsen, Unilateral vibro-impact systems - Experimental observations against theoretical predictions based on the coefficient of restitution, J. Sound Vib. 440 (2019) 346–371. doi:10.1016/j.jsv.2018.10.037.
[58] X. Lyu, Q. Gao, G. Luo, Dynamic characteristics of a mechanical impact oscillator with a clearance, Int. J. Mech. Sci. 178 (December 2019) (2020) 105605. doi:10.1016/j.ijmecsci.2020.105605.
[59] S. Yin, G. Wen, J. Ji, H. Xu, Novel two-parameter dynamics of impact oscillators near degenerate grazing points, Int. J. Non. Linear. Mech. 120 (October 2019) (2020) 103403. doi:10.1016/j.ijnonlinmec.2020.103403.
[60] W. Zhang, F. Min, J. Chen, Y. Dou, Discontinuous Dynamic Analysis of a Modified Duffing-Rayleigh System with a Piecewise Quadratic Function, IEEE Access 8 (2020) 32312–32320. doi:10.1109/ACCESS.2020.2973469.
[61] U. Andreaus, M. De Angelis, Nonlinear dynamic response of a base-excited SDOF oscillator with double-side unilateral constraints, Nonlinear Dyn. 84 (3) (2016) 1447–1467. doi:10.1007/s11071-015-2581-4.
[62] U. Andreaus, P. Baragatti, M. De Angelis, S. Perno, A Preliminary Experimental Study About Two-Sided Impacting SDOF Oscillator Under Harmonic Excitation, J. Comput. Nonlinear Dyn. 12 (6) (2017) 061010. doi:10.1115/1.4036816.
[63] U. Andreaus, P. Baragatti, M. De Angelis, S. Perno, Shaking table tests and numerical investigation of two-sided damping constraint for end-stop impact protection, Nonlinear Dyn. 90 (4) (2017) 2387–2421. doi:10.1007/s11071-017-3810-9.
[64] U. Andreaus, M. De Angelis, Experimental and numerical dynamic response of a SDOF vibro-impact system with double gaps and bumpers under harmonic excitation, Int. J. Dyn. Control 7 (4) (2019) 1278–1292. doi:10.1007/s40435-019-00532-x.
[65] U. Andreaus, M. De Angelis, Influence of the characteristics of isolation and mitigation devices on the response of single-degree-of-freedom vibro-impact systems with two-sided bumpers and gaps via shaking table tests, Struct. Control Heal. Monit. 27 (5) (2020) 1–21. doi:10.1002/stc.2517.
[66] G. Stefani, M. De Angelis, U. Andreaus, Experimental and numerical investigation of base isolated SDOF system impact against bumpers under harmonic base excitation, in: M. Papadrakakis, M. Fragiadakis (Eds.), Proc. 7th Int. Conf. Comput. Methods Struct. Dyn. Earthq. Eng. (COMPDYN 2019), Vol. 2, 2019, pp. 3333–3343. doi:10.7712/120119.7150.19207.
[67] G. Stefani, M. De Angelis, U. Andreaus, Experimental dynamic response of a SDOF oscillator constrained by two symmetrically arranged deformable and dissipative bumpers under harmonic base excitation, in: W. Lacarbonara, B. Balachandran, J. Ma, J. Tenreiro Machado, G. Stepan (Eds.), Nonlinear Dyn. Control, Springer, Cham, 2020, pp. 119–127. doi:10.1007/978-3-030-34747-5_12.
[68] G. Stefani, M. De Angelis, U. Andreaus, Experimental and numerical response analysis of a unilaterally constrained sdof system under harmonic base excitation, in: A. Carcaterra, A. Paolone, G. Graziani (Eds.), Proc. XXIV AIMETA Conf. 2019. Lect. Notes Mech. Eng., Springer, Cham, 2020, pp. 1488–1497. doi:10.1007/978-3-030-41057-5_120.
[69] G. Stefani, M. De Angelis, U. Andreaus, Scenarios in the experimental response of a vibro-impact single-degree-of-freedom system and numerical simulations, Nonlinear Dyn. in press (2020).
[70] A. K. Chopra, Dynamic of Structures: Theory and Applications to Earthquake Engineering, forth edit Edition, Pearson, Englewood Cliffs, New Jersey, 2012.